Technische Universität München
Fakultät für Medizin

Advanced ultra-low-dose CT assessment of bone fracture risks in patient with osteoporosis with novel acquisitions and reconstruction schemes

Kai Mei

Vollständiger Abdruck der von der Fakultät für Medizin der Technischen Universität München zur Erlangung des akademischen Grades eines *Doktors der Naturwissenschaften* genehmigten Dissertation.

Vorsitzende	Prof. Dr. Ulrike Protzer
Prüfende/-r der Dissertation	1. Priv.-Doz. Dr. Peter Noël
	2. Prof. Dr. Franz Pfeiffer

Die Dissertation wurde am 10.04.2019 bei der Technischen Universität München eingereicht und durch die Fakultät für Medizin am 14.08.2019 angenommen.

FAKULTÄT FÜR MEDIZIN

TECHNISCHE UNIVERSITÄT MÜNCHEN

Experimental Medicine (Dr. rer. nat.)
Cumulative Thesis

Advanced CT assessment of bone fracture risks

Kai Mei

FAKULTÄT FÜR MEDIZIN

TECHNISCHE UNIVERSITÄT MÜNCHEN

Experimental Medicine (Dr. rer. nat.)
Cumulative Thesis

Advanced ultra-low-dose CT assessment of bone fracture risks in patient with osteoporosis with novel acquisitions and reconstruction schemes

Fortgeschrittene ultra-low-dose CT Beurteilung des Knochenbruchrisikos von Patienten mit Osteoporose mittels neuartiger Akquisitions und Rekonstruktionsschemata

Author:	Kai Mei
1. Supervisor:	PD Dr. Peter B. Noël
2. Supervisor:	Prof. Dr. Franz Pfeiffer
Mentor:	PD Dr. med. Thomas Baum
Submission Date:	1 April 2019

I confirm that this Experimental Medicine (Dr. rer. nat) cumulative thesis is my own work and I have documented all sources and material used.

Munich, 1 April 2019 Kai Mei

Acknowledgments

First of all, I would like to express my deep gratitude to my supervisor Peter B. Noël for introducing me to the field of computed tomography during my master study and giving me the opportunity to do the doctoral program. During all these years, Peter has been providing me guidance and courage during the pursuit of my dissertation. His valuable support has been of great help during the development of my dissertation and will be continuously cherished in my following career.

My sincere thanks also go to my mentors Thomas Baum and Jan S. Kirschke. Thomas and Jan provided valuable medical knowledge and insightful thoughts for my research field, which were very motivating and helpful to my dissertation. Thomas' patience and suggestions during our numerous discussions are greatly appreciated.

This thesis could not have been completed without the support and contribution from my colleagues. I would like to thank Felix K. Kopp for helping me with all kinds of problems and for all the helpful discussions. I would like to also thank Benedikt J. Schwaiger and Alexandra S. Gersing for their invaluable comments and advice during the making of my journal publications. I am grateful to my current and former colleagues at the office, Manuel Schultheiss, Veronica Bodek, Johannes Hammel and Alexis Laugerette, they have been providing a pleasant atmosphere as well as professional help during the last several years. Thanks should also be given to Nico Sollman for his great work in our mutual projects. My thanks are extended to David Jany, Bernhard Renger and Alexander Valentinitsch. They have been providing support regarding technical problems.

I am particularly grateful for Professor Franz Pfeiffer being my second supervisor. Franz and his E17 group have been providing constant help during my research.

To Andreas Fehringer, who gave me considerable help on the reconstruction code. To Sebastian Allner and Wolfgang Noichl, who offered trouble-shooting whenever I was facing computational and server problems. To Sebastian Ehn, who provided me tremendous support on my last publication. Also thanks to the other members of the E17 team, for their substantial help and influence to my research topics.

In addition, I would like to acknowledge the support from the CT research laboratory of Philips Healthcare. I would like to thank Rolf Bippus and his colleagues for providing resources accessing the raw data in the CT scanner.

Moreover, I wish to thank Professor Ernst Rummeny, the department of radiology, the section of neuroradiology and Klinikum rechts der Isar in Technical University of Munich for providing me the opportunity of working as a researcher during the pursuit of my thesis. In addition, my thanks should be given to the attending physicians and residence doctors in our department for their contributions that were also of great importance during my research.

Last but not least, I want to express my sincere gratitude to my family, for their love, support and comfort whenever I needed the most during my life.

Abstract

As a bone disease, osteoporosis is characterized by low bone mass and deterioration of bone microstructure. It is a common condition for a majority of people as a result of aging. Osteoporotic fractures, as a direct result of untreated osteoporosis, lead to pain, immobility and possibly even fatality for patients, causing a huge cost of medical care, lost of workforce and thus heavy society burden. In most cases, osteoporosis is often only diagnosed when the first fracture occurs.

Computed tomography (CT), as an in-vivo, fast and high-quality medical imaging modality, is particularly well-suited for bone imaging and has the potential to offer osteoporosis screening. However, due to the substantial radiation exposure applied to the patient, Quantitative CT (QCT) for bone mineral density (BMD) has not seen as a standard for osteoporosis screening and monitoring.

This thesis project investigated the potential of low dose and ultra-low dose CT in the context of musculoskeletal CT imaging with novel data acquisition and image reconstruction schemes. In-vivo human subjects (in control and osteoporosis groups) examined with a conventional medical CT were retrospectively collected. An advanced model-based statistical iterative reconstruction (SIR) algorithm was implemented. Low dose scanning protocols were realized by simulating lower X-ray tube current and sparse sampling. BMD and trabecular microstructure were investigated. While the accuracy of identifying healthy and osteoporosis patients depends on the radiation dose, our results showed that the quantification of BMD with sparse sampling was much more reliable compared to lowering X-ray tube current. The results also suggested that the examinations of trabecular microstructure, with both sparse sampling and lowering tube current, were very sensitive to the level of radiation exposure.

In addition, potentials of advanced multi-energy CT for quantitative bone imaging were studied. This research topic was divided into two main aspects: material quantification and decomposition. Both ex-vivo vertebral specimens and in-vivo patient subjects were scanned with a clinical dual-layer CT system. In the first part,

an algorithm was implemented to deliver BMD, by comparing the monoenergetic CT images generated by the scanner with corresponding referencing images of quantitative phantoms. The results showed an excellent correlation with conventionally delivered BMD using QCT. In the second part, a decomposition algorithm was investigated to measure the calcium hydroxyapatite (HA), water and fat fraction within the bone. Comparing to corresponding magnetic resonance (MRI) images, the results suggested that multi-energy CT has the potential over conventional CT to identify acute and chronic fractures through estimating the water and fat bone compositions.

In conclusion, this thesis investigates (1) ultra-low-dose CT for musculoskeletal imaging with novel data acquisition and image reconstruction schemes for osteoporosis screening and (2) clinical applications of advance multi-energy CT: BMD quantification and bone composition estimation.

Zusammenfassung

Osteoporose ist eine häufige Knochenerkrankung, die durch geringe Knochenmasse und Verschlechterung der Knochenmikrostruktur gekennzeichnet ist. Typischerweise wird Osteoporose oft erst mit dem Auftreten einer Fraktur diagnostiziert. Osteoporotische Frakturen führen zu Schmerzen, Immobilität und benötigen daher auch eine aufwendige medizinische Versorgung. Diese Frakturen, die oftmals mit pharmakologischer Therapie vermeidbar sind, stellen jedoch schwere Belastungen, sowohl für die Patienten als auch für die Gesellschaft dar.

Die Computertomographie (CT) ist eine schnelle und zuverlässige Bildgebungsmodalität im klinischen Alltag. Sie eignet sich besonders gut für die Bildgebung der Knochen und bietet daher großes Potenzial zur Früherkennung von Osteoporose. Aufgrund der erheblichen Strahlenbelastung wird die quantitative CT (QCT) für die Messung der Knochendichte jedoch nicht allgemein zur Früherkennung und Nachsorge von Osteoporose durchgeführt.

Die Vorliegende Arbeit befasst sich mit der Anwendung von strahlenreduzierter CT zur Beurteilung des Knochenbruchrisikos. Im Wesentlichen wurden neuartige Akquisitionschemata und Rekonstruktionsalgorithmen entwickelt. Patienten (in Kontroll- und Osteoporosegruppen), die mit einem konventionellen medizinischen CT untersucht worden sind, wurden retrospektiv in die Studien eingeschlossen. Strahlenreduzierte Scanprotokolle wurden durch eine Reduzierung des Röhrenstroms der Röntgenquelle oder durch spärliche Abtastung realisiert. Ein fortschrittlicher Rekonstruktionsalgorithmus (modellbasierte statistische iterative Rekonstruktion, SIR) wurde implementiert um die Bildqualität der strahlenreduzierten Daten zu verbessern. Für die Evaluierung wurde die Dichte und die trabekuläre Mikrostruktur der Knochen untersucht. Die Ergebnisse zeigen, dass mithilfe solcher Verfahren Osteoporose bei Patienten/-innen, selbst unter der Verwendung niedriger Strahlendosis, diagnostiziert werden kann. Des Weiteren wurde gezeigt, dass die Quantifizierung der Knochendichte mit spärlicher Abtastung im Vergleich zur Verringerung des Röhrenstroms zuverlässiger ist. Die Beurteilung der trabekulären Mikrostruktur wurde sowohl bei spärlicher Abtastung als auch bei reduzierter

Stromstärke sehr empfindlich von der Strahlendosis beeinflusst.

Zusätzlich wurde das Potenzial der Multi-Energie CT für die Knochenbildgebung untersucht. Dieses Forschungsthema wurde in zwei Aspekte unterteilt: Materialquantifizierung und -zerlegung. Die Studien wurden an ex-vivo Wirbelkörper und in-vivo Patienten durchgeführt, die mit einem klinischen Dual-Energy-CT gescannt wurden. Ein Algorithmus wurde implementiert, um die Knochendichte zu bestimmen. Hierbei werden die vom Scanner erzeugten monoenergetischen Bilder mit den entsprechenden Referenzbildern quantitativer BMD-Phantome verglichen. Es wurde eine hervorragende Korrelation mit konventionellen Messungen der Knochendichte festgestellt. Im zweiten Teil wurde ein Algorithmus zur Materialzerlegung untersucht, um den Calciumhydroxylapatit-, Wasser- und Fettanteil im Knochen zu messen. Ein Vergleich mit entsprechenden Bildern der Magnetresonanztomographie zeigte, dass Multi-Energie CT das Potenzial hat, akute und chronische Frakturen durch eine Schätzung der Wasser- und Fettzusammensetzung im Knochen zu identifizieren.

Zusammenfassend untersucht diese Arbeit (1) strahlenreduzierte CT Bildgebung mit neuartigen Akquisitions- und Rekonstruktionsschemata zur Früherkennung von Osteoporose und (2) klinische Anwendungen der Dual-Energy-CT: BMD Quantifizierung und Bestimmung der Knochenzusammensetzung.

Abbreviations

AUC	Area under the (receiver operating characteristic) curve
BF	Bone fraction
BMD	Bone mineral density
aBMD	Areal bone mineral density
vBMD	Volumetric bone mineral density
CNR	Contrast-to-noise ratio
CT	Computed tomography
CTDI	(Volumetric) computed tomography dose index
DECT	Dual-energy computed tomography
DLCT	Dual-layer computed tomography
DSCT	Dual-source computed tomography
DXA	Dual-energy X-ray absorptiometry
FBP	Filtered back-projection
FE	Finite element
FFT	Fast Fourier transform
FD	Fractal dimension
FL	Failure load
FOV	Field of view
FT	Fourier transform
HA	(Calcium) hydroxyapatite
KVP	Peak kilo voltage
MDCT	Multi-detector computed tomography
MRI	Magnetic resonance imaging
NIST	(United States) National Institute of Standards and Technology
QCT	Quantitative computed tomography
ROC	Receiver operating characteristic
ROI	Region of interest
SIR	Statistical iterative reconstruction
SNR	Signal-to-noise ratio
SPS	Seperable paraboloid surrogate

SpS	Sparse sampling
TC	Tube current
TbN	Trabecular number
TbSp	Trabecular separation
TbTh	Trabecular thickness
VMI	Virtual monoenergetic image

List of included journal publications

The presented dissertation is based on the following three journal publications:

J-I **K. Mei**, F. K. Kopp, R. Bippus, T. Köhler, B. J. Schwaiger, A. S. Gersing, A. Fehringer, A. Sauter, D. Münzel, F. Pfeiffer, E. J. Rummeny, J. S. Kirschke, P. B. Noël and T. Baum. *Is multidetector CT-based bone mineral density and quantitative bone microstructure assessment at the spine still feasible using ultra-low tube current and sparse sampling?* European Radiology 2017 Dec;27(12):5261-5271. doi: 10.1007/s00330-017-4904-y.

J-II **K. Mei***, B. J. Schwaiger*, F. K. Kopp, S. Ehn, A. S. Gersing, J. S. Kirschke, D. Münzel, A. A. Fingerle, E. J. Rummeny, F. Pfeiffer, T. Baum, P. B. Noël. *Bone mineral density measurements in vertebral specimens and phantoms using dual-layer spectral computed tomography.* Scientific reports 2017 Dec 13;7(1):17519. doi: 10.1038/s41598-017-17855-4.

J-III **K. Mei**, S. Ehn, M. Oechsner, F. K. Kopp, D. Pfeiffer, A. A. Fingerle, F. Pfeiffer, S. E. Combs, J. J. Wilkens, E. J. Rummeny, P. B. Noël. *Dual-layer spectral computed tomography: measuring relative electron density.* European Radiology Experimental 2018 Aug 22;2:20. doi: 10.1186/s41747-018-0051-8.

The above three journal publications are referred as J-I, J-II and J-III respectively.

* First authorship is shared.

Declaration of shared first-author

Benedikt J. Schwaiger and **Kai Mei** contributed equally to the journal publication J-II with the title *BMD measurements in vertebral specimens and phantoms using dual-layer spectral computed tomography*, which was published in Scientific Reports on Dec. 13, 2017.

We agree with the inclusion of this publication in K. Mei's cumulative thesis to attain his degree of Experimental Medicine (Dr. rer. nat.).

PD Dr. med. Benedikt J. Schwaiger

Kai Mei

List of related publications

The author contributed to the following subject-related journal publications:

J-1 F. K. Kopp, T. Baum, R. A. Nasirudin, **K. Mei**, Eduardo G. Garcis, R. Burkart, E. J. Rummeny, J. S. Bauer, and P. B. Noël. *Effect of low-dose and iterative reconstruction on trabecular bone microstructure assessment.* PLoS One. 2016 Jul 22.

J-2 D Anitha, K. Subburaj, **K. Mei**, F. K. Kopp, P. Foehr, P. B. Noël, J. S. Kirschke, T. Baum. *Effects of dose reduction on bone strength prediction using finite element analysis.* Sci Rep. 2016 Dec 9;6:38441.

J-3 K. Mechlem, S. Allner, S. Ehn, **K. Mei**, E. Braig, D. Münzel, F. Pfeiffer, and P. B. Noël. *A post-processing algorithm for spectral CT material selective images using learned dictionaries.* Biomed Phys Eng Express 3, no. 2 (2017): 025009

J-4 S. Ehn, T. Sellerer, D. Münzel, A. A. Fingerle, F. K. Kopp, M. Duda, **K. Mei**, B. Renger, J. Herzen, J. Dangelmaier, B. J. Schwaiger, A. Sauter, I. Riederer, M. Renz, R. Braren, R. J. Rummeny, F. Pfeiffer, P. B. Noël. *Assessment of quantification accuracy and image quality of a full-body dual-layer spectral CT system.* J Appl Clin Med Phys. 2018 Jan;19(1):204-217.

J-5 M. R. K. Mookiah, A. Rohrmeier, M. Dieckmeyer, **K. Mei**, F. K. Kopp, P. B. Noël, J. S. Kirschke, T. Baum, K. Subburaj. *Feasibility of opportunistic osteoporosis screening in routine contrast-enhanced multi detector computed tomography (MDCT) using texture analysis.* Osteoporos Int. 2018 Apr;29(4):825-835.

J-6 M. R. K. Mookiah, T. Baum, **K. Mei**, F. K. Kopp, G. Kaissis, P. Foehr, P. B. Noël, J. S. Kirschke, K. Subburaj. *Effect of radiation dose reduction on texture measures of trabecular bone microstructure: an in vitro study.* J Bone Miner Metab. 2018 May;36(3):323-335.

J-7 M. R. K. Mookiah, K. Subburaj, **K. Mei**, F. K. Kopp, J. Kaesmacher, P. M. Jungmann, P. Foehr, P. B. Noël, J. S. Kirschke, T. Baum. *Multidetector computed tomography imaging: effect of sparse sampling and iterative reconstruction on trabecular bone microstructure.* J Comput Assist Tomogr. 2018 May/Jun;42(3):441-447.

J-8 D. Anitha, **K. Mei**, M. Dieckmeyer, F. K. Kopp, N. Sollmann, C. Zimmer, J. S. Kirschke, P. B. Noël, T. Baum, K. Subburaj. *MDCT-based finite element analysis of vertebral fracture risk: what dose is needed?* Clin Neuroradiol. 2018 Aug 21

J-9 D. Anitha, K. Subburaj, F. K. Kopp, **K. Mei**, P. Foehr, R. Burgkart, N. Sollmann, C. Maegerlein, J. S. Kirschke, P. B. Noël, T. Baum. *Effect of statistically iterative image reconstruction on vertebral bone strength prediction using bone mineral density and finite element modeling - a preliminary study.* J Comput Assist Tomogr. 2018 Sep 10.

J-10 B. J. Schwaiger, A. S. Gersing, J. Hammel, **K. Mei**, F. K. Kopp, J. S. Kirschke, E. J. Rummeny, K. Wörtler, T. Baum, P. B. Noël. *Three-material decomposition with dual-layer spectral CT compared to MRI for the detection of bone marrow edema in patients with acute vertebral fractures.* Skeletal Radiol. 2018 Nov;47(11):1533-1540.

J-11 N. Sollmann, **K. Mei**, B. J. Schwaiger, A. S. Gersing, F. K. Kopp, R. Bippus, C. Maegerlein, C. Zimmer, E. J. Rummeny, J. S. Kirschke, P. B. Noël, T. Baum. *Effects of virtual tube current reduction and sparse sampling on MDCT-based femoral BMD measurements.* Osteoporos Int. 2018 Dec;29(12):2685-2692.

J-12 N. Sollmann, **K. Mei**, D. M. Hedderich, C. Maegerlein, F. K. Kopp, M. Löffler, C. Zimmer, E. J. Rummeny, J. S. Kirschke, T. Baum, P. B. Noël. *Multi-Detector CT imaging: impact of virtual tube current reduction and sparse sampling on detection of vertebral fractures.* Euro Radio. 2018.

J-13 N. Sollmann, **K. Mei**, I. Riederer, S. Schön, F. K. Kopp, J.S. Kirschke, E. J. Rummeny, C. Zimmer, C. Maegerlein, B. Friedrich, K. Kreiser, P. B. Noël, T. Baum. *Tube current reduction in computed tomography angiography – how low can we go in patients with suspected acute stroke?* Am J Roentgenol. 2018. (Accepted, in press.)

J-14 F. Roski, J. Hammel, **K. Mei**, T. Baum, J. S. Kirschke, A. Laugerette, F. K. Kopp, J. Bodden, D. Pfeiffer, F. Pfeiffer, E. J. Rummeny, P. B. Noël, A. S. Gersing, B. J. Schwaiger. *Bone mineral density measurements derived from dual-layer spectral CT enable opportunistic screening for osteoporosis.* Euro Radio. 2019.

J-15 A. P. Sauter, J. Hammel, S. Ehn, K. Achterhold, F. K. Kopp, M. A. Kimm, **K. Mei**, A. Laugerette, F. Pfeiffer, E. J. Rummeny, D. Pfeiffer, P. B. Noël. *Perfusion-ventilation CT via three-material differentiation in dual-layer CT: a feasibility study.* Sci Rep. 2019.

The above journal publications are referred to using J-1 to J-15 respectively.

The author contributed to the following conference publications:

C-1 F. K. Kopp, T. Baum, R. A. Nasirudin, **K. Mei**, et al. *Effect of low-dose and iterative reconstruction on trabecular bone microstructure assessment.* SPIE Medical Imaging 2016

C-2 K. Mechlem, S. Allner, **K. Mei**, F. Pfeiffer and P. B. Noël. *Dictionary-based image denoising for dual energy computer tomography.* SPIE Medical Imaging 2016

C-3 **K. Mei**, F. K. Kopp, A. Fehringer, et al. *Effects of sparse sampling in combination with iterative reconstruction on quantitative bone microstructure assessment.* SPIE Medical Imaging 2017

C-4 **K. Mei**, B. J. Schwaiger, F. K. Kopp, et al. *Calcium decomposition and phantomless bone mineral density measurements using dual-layer-based spectral computed tomography.* SPIE Medical Imaging 2018

C-5 **K. Mei**, F. K. Kopp, J. Hammel, et al. *Advancements in computed tomography for musculoskeletal imaging.* CT Meeting 2018

The above conference publications are referred to using C-1 to C-5 respectively.

Compliance with ethical standards

All investigations performed in studies involving human participants were in accordance with the ethical standards of the institutional and/or national research committee and with the 1964 Helsinki declaration and its later amendments or comparable ethical standards. Informed consent was obtained from all individual participants included in the studies.

All patient images and data in this thesis were collected in Klinikum rechts der Isar, Technical University of Munich.

Contents

Part I.

Research Summary

1. Introduction

1.1. Clinical background and motivation

Osteoporosis is a disease characterized by low bone mass and deterioration of bone micro-architectural tissue. It disturbs the balance of the spine, changes body posture and is associated with an 8-fold increase in mortality [1] [2]. Commonly, osteoporosis has no typical symptoms until an actual fracture occurs. Osteoporotic fractures cause an increasing burden both to the patient and the society [3] [4], despite the fact that osteoporosis is considered as treatable and the fractures are preventable by early initiation of pharmacological therapy. As nowadays people have a longer life expectancy, osteoporosis receives a growing amount of attention. However, in the European Union only 10-15% of patients are treated adequately [1].

The under-diagnosed and under-treated situation of osteoporosis is aggravated by the limited accuracy of standard diagnosis tools. Dual-energy X-ray absorptiometry (DXA), as the only standard clinical method for quantitative imaging of osteoporosis proposed by World Health Organization since the late 1980s, enables the measurement of areal bone mineral density (aBMD, g/cm^2), which is most commonly applied at the lumbar spine and/or proximal femur. However, aBMD is a projection-based measurement which is influenced by the size of the body and the surrounding conditions of tissues, such as calcification in blood vessels or organs. In addition, recent studies have shown that DXA is partly insufficient to identify subjects at high risk of osteoporotic fractures: over half of none vertebral fractures occurred in patients with non-pathological aBMD values, [5] [6], which indicates that trabecular bone microstructure analysis may also be necessary for assessing fracture risk.

As one of the most important medical imaging technique today, computed tomography (CT) is particularly good at bone imaging in the clinical routine, because human bone is dense and absorbs a substantial amount of X-rays, creating

high contrast for diagnosis. By providing the 3D image volumes of the patient's body, quantitative CT (QCT) can measure volumetric bone mineral density (vBMD, mg/cm^3) free from the influences of surrounding soft tissue and blood calcification near the lumbar spine. Moreover, CT can access detail information of in-vivo bone microstructure. It is shown that high-resolution CT improves the prediction of bio-mechanical bone strength and fracture risk beyond aBMD-based DXA, [7] [8] [9]. However, current CT/QCT examination is subject to a high radiation dose and is clinically not acceptable for longitudinal assessment of fracture risk and therapy monitoring [10].

While most of the current CT protocols focus on infrequent abdominal examinations where dose is comparatively of lesser concern, osteoporosis-screening-based CT/QCT examinations are more frequently performed per patient and their radiation dose must be reduced. New scanning protocols and corresponding new acquisition and reconstruction schemes would be very attractive to musculoskeletal CT imaging. In this thesis, sparse-sampling is investigated, a method where the CT switches on and off the X-ray source during the gantry rotation to cut down radiation exposure. In order to mitigate the effects of inadequate data acquired, an advanced reconstruction algorithm, for example, model-based statistical iterative reconstruction (SIR), was used. The study was performed on in-vivo patients (osteoporotic and healthy groups) retrospectively collected. Both BMD and trabecular bone microstructure were analyzed.

Additionally, novel techniques in CT, such as spectral and multi-energy CT, have transferred from academic/manufacturer's prototypes to actual clinical applications. For osteoporosis screening or general musculoskeletal CT imaging, dual-energy CT (DECT) acts as a much more advanced alternative to DXA and conventional QCT. As CT is a much more frequently used imaging modality, DECT has the potential of acting as an opportunistic osteoporosis screening method because it can recognize and quantify specific materials, such as in-vivo bone mineral. This thesis project investigated the performance of a dual-layer based DECT, discussing the studies of material quantification and decomposition in musculoskeletal CT imaging. DECT applications for clinical applications, such as osteoporosis diagnosis without conventional phantoms, distinguishing yellow and red bone marrows and determining their fractions within vertebrae, were evaluated with ex-vivo specimens and/or retrospectively on patient data.

1.2. Study subject in this thesis

This thesis focuses on the CT musculoskeletal imaging. The types of bones studied are briefly introduced in this section.

Human bones are not uniformly solid; the majority of bones have a hard and compact outer layer (cortical bone) and a spongy internal area (cancelous or trabecular bone). Trabecular bone has a higher surface-area-to-volume ratio and provides spaces for metabolic activities as well as structural support. It contains bone marrow, which can be divided into yellow and red marrow depending on their portions of fat cells (adipose-dominated) and blood component (mostly water). The fraction of adipose tissue inside the bone increases as the person ages, which is believed to contribute also to fracture risk. For a bone with fracture, the composition of adipose and water in the bone marrow can indicate the age of the fracture: a fresh fracture often contains excess fluid, which is referred to as a bone marrow edema.

Bone mineral density (BMD) is one of the most important referencing attributes when diagnosing osteoporosis. By definition, BMD describes the amount of bone mineral in bone tissue (mg/cm^3). Bone mineral is formed by calcium hydroxyapatite (HA). In clinical practice, BMD measured in QCT is technically the translated value from the X-ray attenuation intensity (Hounsfield Units, HU) within the areas of trabecular bone by comparing the reference scans of phantoms containing actual concentrations of HA. This translation is commonly referred to as calibration.

In this thesis, trabecular bone microstructure refers to the characteristic appearance of the trabeculae within the bone marrow. This appearance is represented by descriptive parameters: bone fraction (bone volume over total volume), trabecular separation (average distances between trabeculae), trabecular number (average number of trabeculae per millimeter) and trabecular thickness.

The most mentioned study subject in this thesis is the human spine. It consists of 33 individual bones stacked one on top of each other. They are called vertebrae and can be numbered and categorized according to their locations, Figure 1.1.

Vertebrae connecting the skull, located around the neck, are cervical vertebrae and numbered from C1 to C7. C1 and C2 have special shape compared to the other vertebrae, offering the nodding and shaking motion of the head.

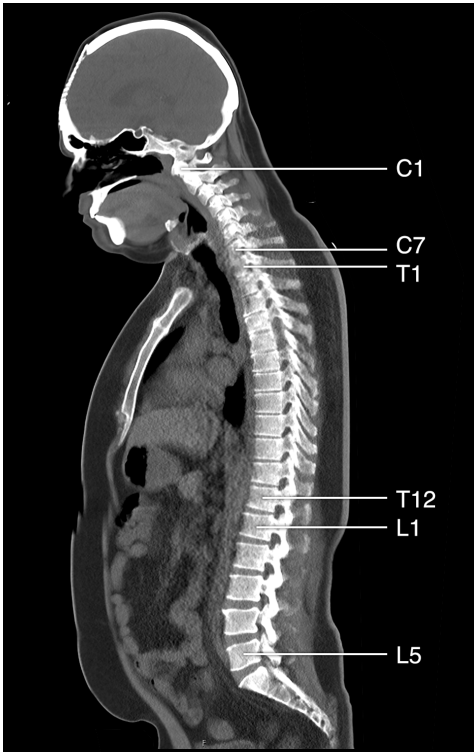

Figure 1.1.: Human spine.

The human spine has 7 cervical vertebrae (C1-C7), 12 thoracic vertebrae (T1-T12) and 5 lumbar vertebrae (L1-L5).

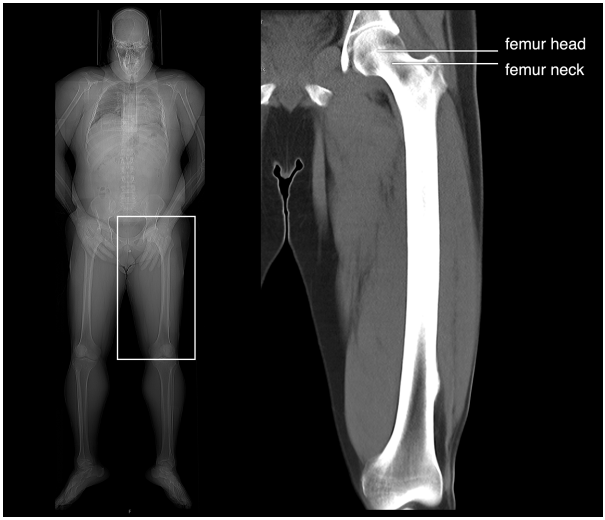

Figure 1.2.: Human femur.

In the middle are thoracic vertebrae numbered from T1 to T12. They are connected to the ribs and hold the rib cage, protecting the heart and the lungs.

Following are the lumbar vertebrae, which are usually the main interest in osteoporosis for one of their crucial functions is to bear the weight of the upper body. They are numbered from L1 to L5. Most QCT examinations involve the lumbar spine.

The rest of the human vertebrae (sacrum and coccyx) are fused and not movable. They are not the focus in this thesis.

The other bone site mentioned in this thesis is the human femur, which is the only bone located in the human thigh, connecting the hip and the knee, Figure 1.2. By most measurements, the femur is the strongest bone in the body and of great clinical significance. Associated with osteoporosis, a hip fracture may involve the fracture of the femur head, femur neck and/or the shaft of the femur. Hip fracture is a common osteoporotic fracture causing mobility problems for elderly people.

1.3. Thesis structure

In Part I of this thesis, Chapter 2 briefly introduces the physics of CT and its reconstruction algorithms. Sparse-sampling CT as a dose reduction technique and its application in osteoporosis screening is discussed in Chapter 3. Chapter 4 provides information on multi-energy CT in musculoskeletal imaging. In Part II, journal publications are summarized.

2. Computed tomography

This chapter briefly introduces the CT data acquisition and image reconstruction.

2.1. Data acquisition

In a common medical CT system, the X-ray light source generates X-rays towards the patient, which pass through and are attenuated by the patient's body, arriving in the end at the detector and being converted to an electronic signal, Figure 2.1. The physics of X-ray attenuation from the patient will be discussed in Chapter 4.1. By comparing the attenuated signals captured at the detectors to the non-attenuated X-ray, information of the objects that the X-ray penetrates through can be recovered, thus revealing anatomical structure inside the human body.

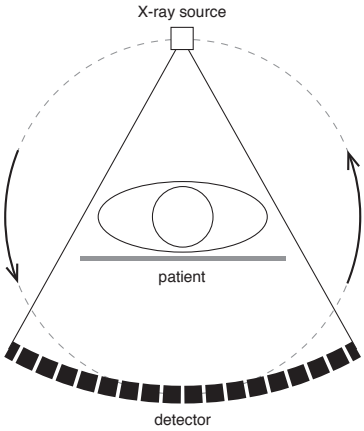

Figure 2.1.: Computed tomography.

In a sequential CT scan, the gantry (X-ray source and detector units) rotates 360° and after that, the patient table moves forward. In an helical scan, the gantry rotates while the patient table moves simultaneously into the rotating gantry.

In most cases, the detector plane is considered as a cylindrical plane, Figure 2.2, consisting of a matrix of small detector units. We defined that the X-ray source is positioned at S, the rotation center is at O and the central light starts from S, passes O and arrives to the detector at D. Normally, the center of a cylindrical curve is the X-ray source point S, thus the distance from the source to detector is equal to the radius of the cylinder. The opening angle is noted as ψ.

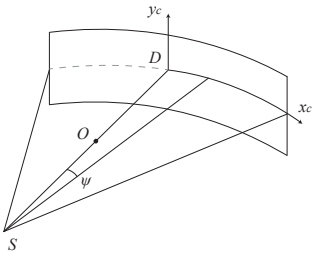

Figure 2.2.: X-ray source and curved detector.

The X-ray source is located at S and emits a cone beam to a cylindrical detector x_c, y_c.

It is mathematically less efficient to handle computations with a cylindrical detector because a curve is a quadratic function. In this thesis, the curved detector is converted to a flat detector, Figure 2.3. For any point (x_c, y_c) at the curved detector, there is a unique point (x_f, y_f) on a flat plane, which is the projection of (x_c, y_c), such that S, (x_c, y_c) and (x_f, y_f) are on the same line. The location of (x_f, y_f) can be computed with:

$$\begin{aligned} x_f &= d \tan \psi, \\ y_f &= y_c / \cos \psi, \end{aligned} \tag{2.1}$$

where $\psi = x_c/d$. d is the distance between the source and the detector. This conversion allows us to treat curved detector CT as if its detector is flat, making the subsequent implementation computationally simpler.

The X-ray emitted from the source is attenuated by the patient's body, following

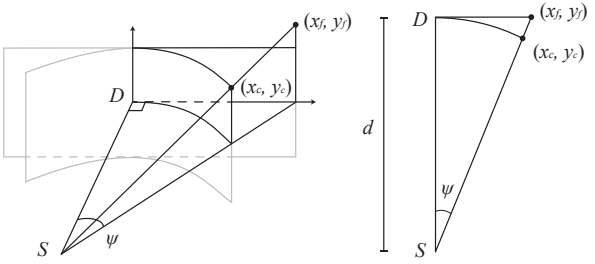

Figure 2.3.: Conversion from curve to flat detector.

For any point at the curved detector (x_c, y_c), a conversion to a flat detector is made by projecting this point to a flat plane (x_f, y_f).

by Beer-Lambert's law, Equation 2.2:

$$I = I_0 \exp(-\int_{\mathrm{x}} \mu(x,y) d\mathrm{x}), \tag{2.2}$$

where $\mu(x,y)$ is the linear attenuation coefficient, i.e. the patient (image), I_0 and I are the intensities of the X-ray beam before and after passing through the patient, x are pixels along the ray path. This can also be represented in logarithm form:

$$g = \ln \frac{I_0}{I} = \int_{\mathrm{x}} \mu(x,y) d\mathrm{x}. \tag{2.3}$$

From the above equation, we observe that the signal g recorded at the detector can be seen as a discrete summation of intensities of the image (attenuation profile). If we assume a ray parallel to the x-axis with distance R to the origin, which can be written as $y = R$, the signal $g(R)$ at the detector located at R, is the integral of the intensities of all the pixels along the line in the image $\mu(x,y)$, Figure 2.4:

$$g(R) = \iint_{x,y} \mu(x,y)\delta(y-R) dx dy. \tag{2.4}$$

Similarly, an X-ray beam with θ between y-axis and distance R to the origin O can be represented with:

$$x\cos\theta + y\sin\theta = R, \tag{2.5}$$

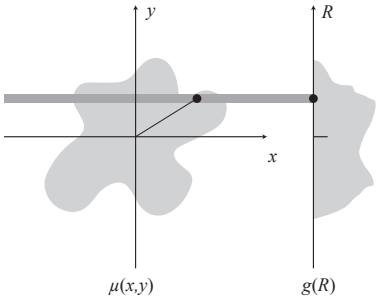

Figure 2.4.: Forward projection of $\mu(x, y)$ for ray $y = R$.

Pixel intensities along the ray in $\mu(x, y)$ sums up to the signal at the detector position R.

yielding a projection (Figure 2.5):

$$g(R, \theta) = \iint_{x,y} \mu(x, y)\delta(x \cos\theta + y \sin\theta - R)dxdy. \tag{2.6}$$

By definition, a collection of $g(R, \theta)$ is called sinogram. Equation 2.6 is called Radon transformation [11], which we note as the forward projection from the image domain to sinogram domain. The inverse operation of this procedure,

$$f(x, y) = \iint_{R,\theta} g(R, \theta)\delta(x \cos\theta + y \sin\theta - R)dRd\theta, \tag{2.7}$$

is referred to as back-projection. Of note, the result of back-projection, $f(x, y)$, is not the forward projected image $\mu(x, y)$. To produce the correct image, image reconstruction algorithms (inverse Radon transformation) are needed, which are discussed in the following sections in this chapter.

In a more realistic situation where the X-ray source is considered as a point source, the scanner geometry is referred to as fan-beam geometry, Figure 2.6. Fan-beam geometry requires the source-to-center distance d' and the source-to-detector distance d. Any ray emitted from the X-ray source while at θ with an opening angle ψ to the detector center, can be represented as:

$$x \cos(\theta + \psi) + y \sin(\theta + \psi) = d' \sin\psi. \tag{2.8}$$

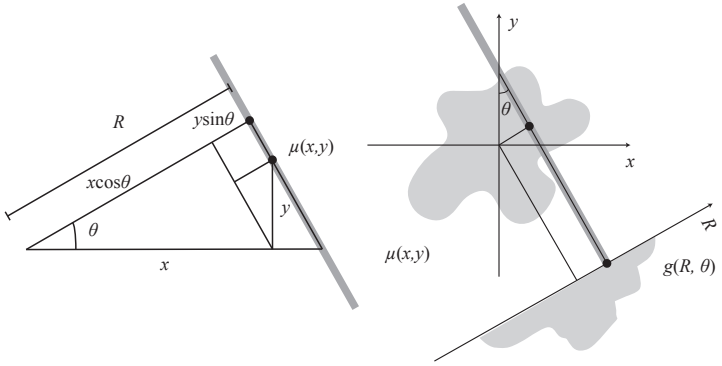

Figure 2.5.: Forward projection of $\mu(x, y)$ for a ray with θ.

In a 2D parallel beam case, forward projection of the ray ($x\cos\theta + y\sin\theta = R$) sums up the pixel intensities, yielding the projection $g(R, \theta)$.

And the forward projection $g(R, \theta)$ is:

$$g(R,\theta) = \iint_{x,y} \mu(x,y)\delta(x\cos(\theta+\psi) + y\sin(\theta+\psi) - d'\sin\psi)dxdy, \qquad (2.9)$$

where $\psi = \arctan(R/d)$.

2.2. Analytical reconstruction algorithm

In mathematics, it requires the central slice theorem [12] to compute $\mu(x, y)$ from sinogram $g(R, \theta)$. The central slice theorem states: the 1D Fourier transform (1D-FT, $\mathbf{FT_1}$) of a projection $g(R, \theta)$ with respect to R is the 2D Fourier transform (2D-FT, $\mathbf{FT_2}$) of $\mu(x, y)$ evaluated at angle θ.

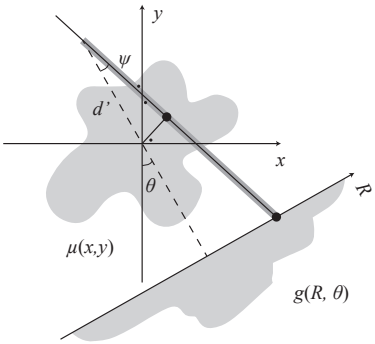

Figure 2.6.: Forward projection of $\mu(x, y)$ at θ in fan-beam geometry.

In 2D fan-beam geometry, rays can be represented analogously with Equation 2.8 and the corresponding forward projection with Equation 2.9.

The 1D-FT of $g(R, \theta)$, from Equation 2.6 with respect to R is:

$$\begin{aligned} G_\theta(\rho) &= \mathbf{FT_1}\{g_\theta(R)\} \\ &= \iiint \mu(x,y)\delta(x\cos\theta + y\sin\theta - R)\exp(-i2\pi R)dxdydR \\ &= \iint \mu(x,y)\exp(-i2\pi\rho(x\cos\theta + y\sin\theta))dxdy \\ &= \iint \mu(x,y)\exp(-i2\pi(\rho\cos\theta x + \rho\sin\theta y))dxdy. \end{aligned} \tag{2.10}$$

And the 2D FT of $\mu(x, y)$ is:

$$\begin{aligned} M(u,v) &= \mathbf{FT_2}\{\mu(x,y)\} \\ &= \iint \mu(x,y)\exp(-i2\pi(ux + vy))dxdy. \end{aligned} \tag{2.11}$$

The above two equations 2.10 and 2.11 are equal, if we write $(u,\ v)$ in polar coordinates ($\rho\cos\theta$, $\rho\sin\theta$). u and v are axes from the frequency domain while x and y axes are from image domain.

$$\begin{aligned} M(u,v) &= \iint f(x,y)\exp(-i2\pi(\rho\cos\theta x + \rho\sin\theta y))dxdy \\ &= G_\theta(\rho). \end{aligned} \tag{2.12}$$

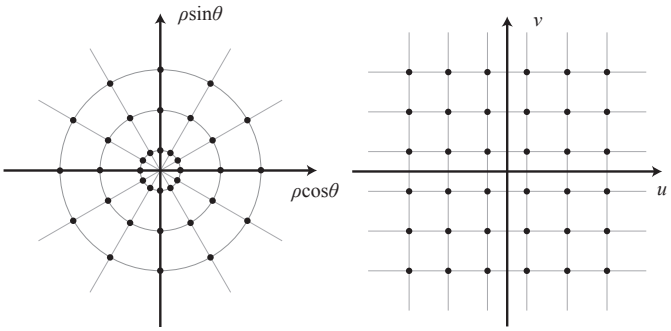

(a) $G(\rho, \theta)$ **(b)** $\mu(u, v)$

Figure 2.7.: Polar grid and Cartesian grid.

The sample points in polar coordinate (left) are to be interpolated into Cartesian coordinate (right).

Thus, a reconstruction of $\mu(x, y)$ from $g(R, \theta)$ can be made by:

$$\mu(x, y) = \mathbf{FT_2^{-1}}\{\mathbf{FT_1}\{g_\theta(R)\}\}. \tag{2.13}$$

$\mathbf{FT_2^{-1}}$ denotes the operation of inverse 2D-FT. Before this, the 1D-FT results of $g(R)$ at different angular positions of θ, as vectors, need to be sliced through origin, re-sampled from polar coordinate (R, θ) to Cartesian coordinate for the inverse 2D-FT, Figure 2.7.

However, because of the computational complexity and memory consumption of inverse 2D-FT, central slice theorem is rarely in practical use. In current modern CT system, filtered back-projection (FBP) is the most used algorithm in clinical routine because of its simplicity and efficiency.

FBP modifies the order of the steps in central slice theorem [13]. It includes the following procedures:

1. Apply a 1D-FT on the projection data to convert to the frequency domain.

$$G_\theta(\rho) = \mathbf{FT_1}\{g_\theta(R)\}\}. \tag{2.14}$$

2. Apply the signal in frequency domain with a high-pass filter, for example,

Ram-Lak filter $|\rho|$ [14] to reduce low frequency signal.

$$G'_\theta(\theta) = |\rho| G_\theta(\rho). \tag{2.15}$$

3. Apply an inverse 1D-FT on the filtered data back to the spatial domain.

$$g'_\theta(R) = \mathbf{FT}_\mathbf{1}^{-\mathbf{1}}\{G'_\theta(\rho)\}. \tag{2.16}$$

4. Superimpose the filtered projections back to the pixels along its ray paths, which is simply back-projecting, Figure 2.8.

$$\mu(x, y) = \iint g'(R, \theta)\delta(x\cos\theta + y\sin\theta - R)dRd\theta. \tag{2.17}$$

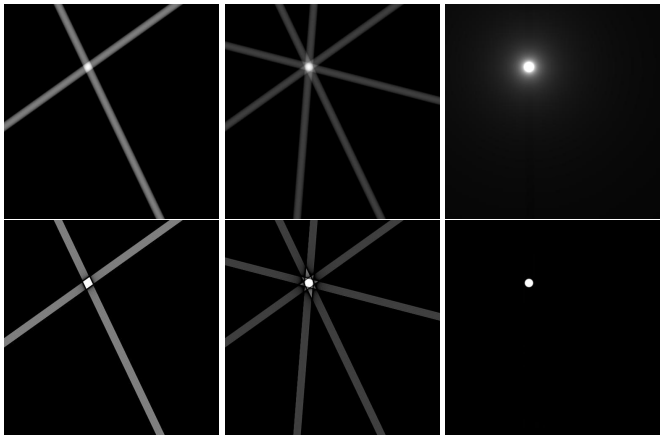

Figure 2.8.: Back-projection and filtered back-projection

Top row: direct back-projection of unfiltered projections. Lower row: back-projection of filtered projections. Back-projection without filtering creates blurred object boundaries, while filtering applies convolution to remove blurring. Filtered back-projection is the primary method in CT image reconstruction.

In practice, several modifications and improvements are made in FBP with respect to real clinical situations. Image denoising is used on the sinogram before and/or after the filtering. The high-pass filter is altered to suppress high frequency signal as it is usually dominated by noise. After the back-projection, various image

improvement techniques, such as edge sharpening and conditional blurring, can be applied to enhance the image contrast or readability with respect to different diagnostic purposes.

Although for helical reconstructions the algorithm is mainly the same, some additional considerations need to be taken [15]. When back-projecting, for each pixel in the image, it required X-rays passing this pixel evenly from all directions. Because the patient table is moving and the X-ray light source has the shape of a cone, some areas of the patient may have redundant X-rays at some spatial directions passing through and some areas far away from the rotation center may lack some X-rays at some specific directions. In this thesis, weighting is added to reduce spatial redundancy and interpolation is implemented for missing directions by taking information from adjacent regions. As a result of this interpolation, the field of view in helical scans is limited by the distance of the table movement during one gantry rotation.

2.3. Model-based iterative reconstruction algorithm

Model-based statistical iterative reconstruction (SIR) is an algorithm which considers the actual projection model and detector statistic. It repeats forward and back projection multiple times in order to compute the image. Historically, it was proposed as early as the analytical reconstruction [16] [17] but was limited to low resolution applications as it requires long computation time and extensive memory capacity. With the current computational power, especially the development of highly parallel computing units such as graphic cards, iterative reconstructions become possible for academic and sometimes clinical applications [18] [19]. Nevertheless, the computation time is still significantly longer than the time for FBP based algorithms. The general scheme of iterative reconstruction is depicted in Figure 2.9.

The steps of Separable Paraboloid Surrogate (SPS) [20], one of the SIR algorithms, is generalized as follows:

1. Initialize an image of attenuation profile, which can be the FBP image or an empty image filled with zeros.

$$\mu^0(x, y) = \mathbf{0}. \tag{2.18}$$

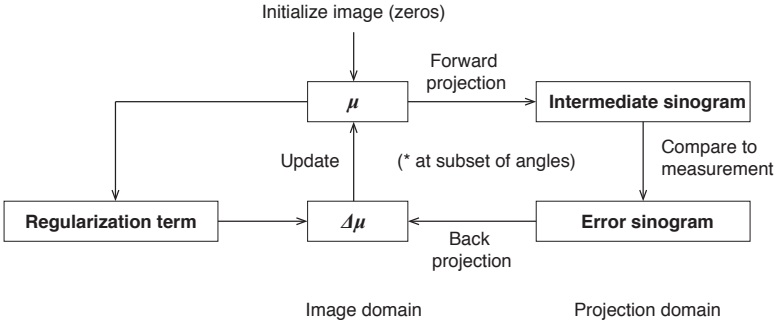

Figure 2.9.: Model-based iterative reconstruction

Model-based iterative reconstruction iterates between the image μ and its projected errors in the sinogram space, compared to the measurement. Each iteration involves a forward projection and a back-projection.

2. Forward-project the current image to projection domain.

$$g^{(i)}(R,\theta) = \iint \mu^{(i)}(x,y)\delta(x\cos\theta + y\sin\theta - R)dxdy. \tag{2.19}$$

3. Compute the difference between the current projection against the measurement (sinogram recorded in scanner). Here the measurement y_0 refers to the intensity of the detected X-ray beam.

$$\Delta g(R,\theta) = I_0 \exp(-g^{(i)}(R,\theta)) - y_0(R,\theta). \tag{2.20}$$

4. Back-project the difference in projection domain to the image domain.

$$\Delta\mu'(x,y) = \iint \Delta g(R,\theta)\delta(x\cos\theta + y\sin\theta - R)dRd\theta. \tag{2.21}$$

5. Normalize the back-projected difference by

$$\Delta\mu = \frac{\Delta\mu'}{d^{pc}}. \tag{2.22}$$

$d^{pc}(x, y)$ is pre-computed curvature. Pre-computed curvature is constant and calculated before the iteration:

$$a(R, \theta) = \iint \delta(x \cos\theta + y \sin\theta - R) dx dy, \tag{2.23}$$

$$d^{pc}(x, y) = \iint a \cdot y_0 \cdot \delta(x \cos\theta + y \sin\theta - R) dR d\theta. \tag{2.24}$$

6. Update the current image using the difference in image domain.

$$\mu^{(i+1)} = \mu^{(i)} + \Delta\mu. \tag{2.25}$$

7. Go back to the step 2 until convergence, i.e. the image μ does not change.

In practice, there are several optimizations for actual implementation:

First of all, the forward- and back-projection are not computed at all angles θ, because it brings extreme heavy computation and also slows down the convergence. Instead of using all angles, only a subset of the angles are visited in each iteration. According to previous experience, if there are 2400 projected angles in one full gantry rotation, this thesis uses 100 angles as a subset (roughly about 1/24) per iteration: during one iteration, 100 angles out of the total 2400 possible angles are randomly selected and performed in Step 2 and 4. For the next iterations, another different 100 angles are chosen. In the end, after a defined number of iterations, all 2400 angles are used evenly during the whole reconstruction process.

In addition, iterative reconstruction is a mathematically ill-posed problem. To improve the convergence of an ill-posed problem and thus to enhance the appearance of the reconstructed image, SIR applies a regularization term [21]. This regularization modifies the update in the image domain such that fewer iterations are needed and that the reconstructed image has reduced noise. To compute the regularization term, an edge preserving function is used, for example, Lange's function [22],

$$\psi(t) = \delta^2[|t/\delta| - \log(1 + |t/\delta|)], \tag{2.26}$$

or Huber penalty [23][15],

$$\psi(t) = \begin{cases} t^2/2, & |t| \leq \delta, \\ \delta|t| - \delta^2/2, & |t| > \delta, \end{cases} \tag{2.27}$$

where t is the intensity difference of the pixel and its neighboring pixels. δ is a threshold indicating the minimal intensity difference between two distinguishable objects.

In summary, considering regularization, each update step for the image can be summarized in Equation 2.28 [24]:

$$\mu^{(i+1)} = \left[\mu^{(i)} + \frac{\mathrm{BP}'[I_0 \exp(-\mathrm{FP}'[\mu^{(i)}]) - y_0] - \beta \sum_K \omega_{jk} \dot{\psi}(\mathrm{x}_j - \mathrm{x}_k)}{\max(d^{pc} + \beta \sum_K \omega_{jk} \ddot{\psi}(\mathrm{x}_j - \mathrm{x}_k), \epsilon)}\right]^+. \quad (2.28)$$

In this equation, $\mathrm{FP}'[\cdot]$ and $\mathrm{BP}'[\cdot]$ indicate forward- and back-projection (Equation 2.6 and 2.7) in a subset of all θ. $\mu^{(i)}$ and $\mu^{(i+1)}$ are the images at step i and $i+1$. y_0 is the measured sinogram. I_0 is the X-ray beam intensity. d^{pc} is the pre-computed curvature.

β controls the strength of the regularization term R,

$$R = \sum_K \omega_{jk} \psi(\mathrm{x}_j - \mathrm{x}_k). \quad (2.29)$$

$\psi(\cdot)$ is the penalty function (Equation 2.26 or 2.27). $\dot{\psi}(\cdot)$ and $\ddot{\psi}(\cdot)$ are its first and second derivatives. x_k is one of the neighboring pixels of x_j in the neighborhood K. K is a 8-pixel neighborhood in a 2D image or 26-pixel in 3D image. ω is the inverse of the distance between x_j and x_k (1, $1/\sqrt{2}$ or $1/\sqrt{3}$).

ϵ is a very small constant ensuring the numerical stability of the iteration. $[\cdot]^+$ means truncation process of negative numbers.

Pseudo code for SIR can be summarized as follows:

/*Statistical Iterative Reconstruction*/
$a \leftarrow \mathrm{FP}[1]$
$d^{PC} = \mathrm{BP}[a \cdot y_0]$
$\mu \leftarrow$ initial reconstruction
for $i = 1$ to max iteration, n_{iter} **do**
  for $m = 1$ to number of subsets, m_{sub} **do**
    $l \leftarrow \mathrm{FP}[\mu]$
    $h \leftarrow I_0 \exp(-l) - y_0$
    $\dot{L} \leftarrow \mathrm{BP}[h]$
    compute $\dot{R}$ and $\ddot{R}$
    $\mu \leftarrow \left[\mu + \frac{\dot{L} - \beta \dot{R}}{\max\{d^{PC} + \beta \ddot{R}, \epsilon\}}\right]^+$

12: **end for**
13: **end for**

Of note, because the algorithm iterates multiple times between the image- and projection domain, it is required that the whole field of view is covered to ensure that no information is lost between the projections. This may cause problems in practice when the X-ray cone-beam does not fully cover the patient body due to relatively large patient size or the detector is not wide enough to record the complete fan angle. Nevertheless, the image μ^i should include everything between the source and detector, which limits the resolution of the reconstructed image because for smaller pixels the image matrix is extremely large. For numerical accuracy, the voxel size in the image space should be also comparable to the pixel size at the detector, thus there is no extra data loss when performing forward and back-projections.

3. Sparse sampling computed tomography

Combined with iterative reconstruction, sparse sampling is a promising technique to further reduce radiation dose in clinical CT examinations.

In the first section, the general idea of sparse sampling CT is introduced. The second section summarizes the clinical research and application regarding osteoporosis screening with sparse sampling. Ongoing and unpublished work is briefly described in the third section.

3.1. Motivation of sparse sampling computed tomography

The main purpose of sparse sampling is saving radiation dose applied to the patient. This chapter starts by explaining the meaning of dose in CT. Although how much X-rays are actually absorbed by patient largely depends on the size of the body and what organs are being examined, the manageable radiation exposure is controlled by manipulating the generation of X-ray and the rotation of the gantry, namely the definition of the scanning protocol. The most important parameters related to the generation of X-rays are tube potential and tube current. The rotation of the gantry is described mainly by rotation speed and table speed (or spiral pitch factor).

Tube potential, also known as peak kilo voltage (kVp), determines the energy and intensity of electrons hitting the anode [25] at the X-ray tube and defines the maximum energy of the generated X-ray photons. Analogical to visible light, tube potential determines both the color and intensity of the X-ray. The generated X-ray beam is not a monochromatic beam. If tube potential is 120 kVp, a range of up to 120 keV X-ray photons can be released. Kilo electron volt, keV, is unit of energy equal to 1.6×10^{-19} joules. Higher energy X-ray is easier to be scattered, and low energy X-ray is easier to be absorbed. Thus, tube potential is not the primary factor controlling radiation dose. All energy photons contribute to the dose applied to the

patient.

Tube current, measured in milliampere (mA), determines the intensity of the X-ray beam or the number of X-ray photons emitted from the X-ray tube. It is the main attribute influencing the trade-off between radiation dose and image quality. Attenuated by the object, X-ray photons are either absorbed or scattered. After that the remaining X-ray photons are converted into visible light photons and hence electronic signals at the detector unit. A certain level of electronic noise occurs during this conversion. When the tube current is high, enough X-ray photons reach the detector, the portion of electronic noise is dismissible and the image quality is better.

The *rotation speed* is described with the rotation time (in seconds) used during the CT rotating one full round. Clinical CT systems, for example, Philips iCT (Philips Healthcare, Best, the Netherlands), has 2400 sampling projection points per rotation in most clinical protocols. The reduction of rotation speed is commonly restricted by the the read-out speed of the detector.

In helical scans, *spiral pitch factor*, or pitch, is a parameter that reflects how fast the patient's table is moving towards the gantry. It is by definition, the table movement per rotation (mm) over the total collimation width (mm), which can also be understood as the percentage movement of the detector plane after one complete gantry rotation. A smaller pitch means that the patient's body is more repeatedly radiated with X-ray. A large pitch means the table moves very fast and also a lower radiation dose. Pitch has an influence to the field of view, large pitch means smaller field of view, because the X-ray beam being a cone-shape beam and cannot cover certain area of the patient far from the rotation center, leading to failing image reconstruction in outer areas.

In a sequential scan, the *exposure time* of one axial slice is the rotation time per one gantry rotation. In helical scans, the exposure time of one axial slice is by definition the rotation time per one gantry rotation over the spiral pitch factor. This is due to the fact that in cone beam helical scans, part of the information gathered in one axial slice can be used in subsequent axial slices. Thus for each axial slice, the exposure time is the averaged time needed when X-ray is applied to the patient.

Finally, the radiation dose, *exposure* of one axial image of the patient, is defined as the product of tube current and exposure time. It has the unit of mAs. This value can be converted to more physiological meaningful values such as gray (Gy) or

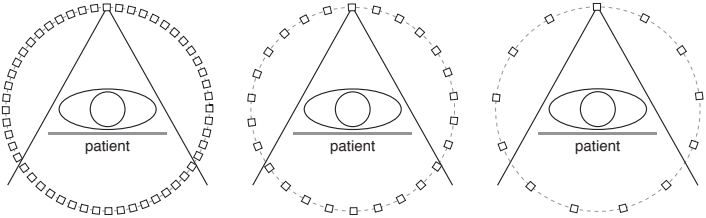

Figure 3.1.: Sparse sampling CT

Left: full sampling CT. Middle: 50% sparse sampling. Right: 25% sparse sampling. In 25% sparse sampling CT, X-ray only emits at 1/4 of the angular positions.

sievert (Sv). The unit gray is defined by how much joule energy is absorbed per kilogram water. CT manufacturers use a water phantom to automatically produce volumetric dose value (mGy) from mAs in the dose report after each scan. The unit sievert is defined by how much joule energy is absorbed by biological tissue. Sievert can only be estimated and is object-specific, considering which different biological organ has different absorption behavior to X-ray. In the following of this thesis, milliampere-second product (mAs) is mostly used to describe radiation dose.

In conventional medical CT, the X-ray source is always on and continuously emitting X-ray to the patient. The exposure has a direct effect to the CT image quality because it is determined only by the tube current, which is the X-ray beam intensity.

On the other hand, sparse sampling CT aims at cutting down the exposure time. Sparse sampling refers to a technique where the X-ray source is switching on and off during the gantry rotation, pulsing the X-ray light source specifically during some positions in the gantry rotation. Compared to conventional CT, sparse sampling CT shoots X-rays at one sampling point after a few angular positions, Figure 3.1. In this thesis, 50% (or 2-times) sparse sampling means the CT takes every second projection a sampling point, compared to full sampling CT. 25% sparse sampling takes every 4th projection as a sampling point. By taking fewer sampling points during the gantry rotation, the exposure time and thus the total radiation exposure is reduced, Table 3.1.

It has certain benefit to reduce sampling points in low-dose CT examinations.

Table 3.1.: Sparse sampling CT lowers radiation exposure.

	continuous	2-times sparse	4-times sparse
Exposure time per rotation	1 s	0.5 s	0.25 s
X-ray tube current (mA)	**200**	**200**	**200**
Exposure (mAs)	200	100	50

Sparse sampling can lower the total effective dose while keeping the tube current high.

By making 1/2 sparse sampling CT, we can shoot twice as strong intensity X-ray in each sampling point, while in the end the radiation dose is the same as the conventional CT, Table 3.2. The signal obtained in each sampling is of high quality and has significantly less electronic noise compared to the sampling points of conventional full-sampling CT.

Table 3.2.: Sparse sampling CT provides X-rays with high tube current.

	continuous	2-times sparse	4-times sparse
Exposure time per rotation	1 s	0.5 s	0.25 s
X-ray tube current (mA)	200	400	800
Exposure (mAs)	**200**	**200**	**200**

Sparse sampling allows high intensity X-ray beam while keeping the total effective radiation dose the same.

Certain artefacts in the reconstructed image will appear if sparse sampling is applied. The most prominent artefacts in the image are aliasing stripes, Figure 3.2. While commonly used reconstruction algorithm in clinical CT (FBP) cannot handle these artefacts, SIR shows great potential because it performs multiple times the forward and back-projection procedure. In addition, stronger regularization can smooth out such aliasing artefacts [26].

The following section discusses related research of sparse sampling CT. This thesis focuses on the SIR implementation and performance on sparse sampling CT, in the context of musculoskeletal imaging. Actual medical problems will be discussed in the subsequent sections, regarding trabecular bone microstructure and actual spine fractures.

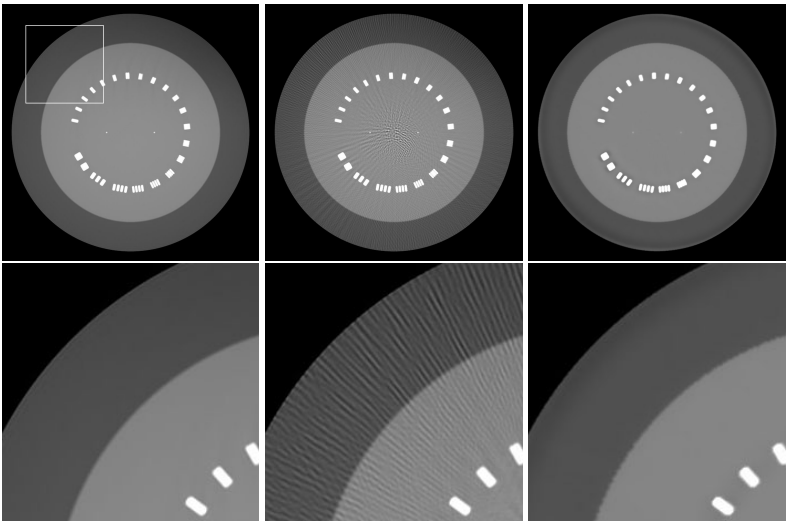

Figure 3.2.: Sparse sampling CT with half dose (50%)

Left: the correct image of a Catphan phantom. Middle: FBP reconstructed Catphan phantom with 1/5 sparse sampling. Right: SIR reconstructed with 1/5 sparse sampling. Note that the regularization in SIR mitigates the aliasing artefact. These images are referenced from J-I

3.2. Related work with sparse sampling computed tomography

Sparse sampling is not possible for current medical CT system because there is no extra unit to switch off the X-ray generator during the gantry rotation. However, the possibility of adding such unit is investigated and the implementation is arguably not impossible [27]. Current existing vascular CT using gridding technique has comparable speed to suppress the X-ray generation [28] [29]. In a prototype of an X-ray generator used in multi-source CT [30], an extraction grid is used on top of the cathode that enables ultra-fast modulation in microsecond range, which will be capable of generating short-enough pulses for sparse sampling CT.

How sparsely the sampling in CT can go was investigated [31]. The number of sampling points mathematically sufficient for reconstruction depends on the scanned subject and the collimation width of the detector. For SIR reconstruction combining proper regularization, simulation studies indicated that as low as 64-views yield accurate appearing images [32] [33]. However, the reconstruction algorithms need to be highly optimized and dedicated [26] [34]. Meaningfulness of this trade-off between radiation dose and image quality largely depends on the actual clinical application.

Different sparse sampling schemes have been studied [35] [36], including (1) regularly sampling of one projection after every few angles; (2) regularly sampling of a bundle of projections after every few angles and (3) sampling in different rows or columns in every projection angles (without switching off the X-ray tube). These studies used micro-CT data taken from a water phantom and mouse heads. The result showed that regularly sampling of one projection after every few angles (1) is the best sparse sampling scheme.

Sparse sampling has seen in actual laboratory set-ups of small flat-panel-detector cone beam CT system [37] [38] [39]. In these applications, task-driven reconstruction algorithms were specifically implemented based on SIR [40] [41].

An actual implementation on medical CT using interrupted beam was implemented and investigated [42] [43] [44]. These studies sampled X-ray in different rows of the detector plane (3), by stopping or splitting the X-ray before it reached the patient by using a multi-slit collimator at the source.

3.3. Sparse sampling in musculoskeletal imaging

The application of iterative reconstruction for sparse-sampling CT in musculoskeletal imaging was investigated with several clinical topics in this thesis.

Ex-vivo vertebral specimens were examined and its iteratively reconstructed images were evaluated prior to the start of this project (**journal publication J-1**). During this preliminary study, the implemented SIR was tested on normal and high-dose CT scans. Trabecular microstructure within the vertebrae was inspected and compared to the maximum fracture load of the bio-mechanical test of the same specimens. The settings of the SIR (both low and high regularization) were investigated. The ratio of bone volume over total volume in the SIR image correlate well with the actual fracture load in low dose scan, indicating the feasibility of SIR in low dose musculoskeletal CT imaging.

In the following of this section, studies on in-vivo experiments are discussed. The first part is focusing on the human spine (vertebrae). The second part focuses on the femur. Spine and femur are both of great importance for radiologists not only because of the frequent fractures but also because fractures that occur on these sites can substantially effect the life quality of patients.

3.3.1. Trabecular structure and bone strength evaluation in vertebrae

The first study was performed regarding the trabecular microstructure reconstructed with SIR for sparse sampling ultra low dose CT (**journal paper J-I**).

In this project, 24 low-dose patient scans were retrospectively collected. These patients underwent routine thoracic and abdominal CT scans (Philips iCT, Philips Healthcare, Best, the Netherlands). Among them, 12 subjects contained osteoporotic fractures and the other 12 control patients had no fractures or metabolic bone changes were selected and paired with the same gender and age (50% female, average age: 73.4 ± 10.8, min 55, max 89). Their raw projection CT data were exported from the scanner and processed on a reconstruction server.

The patient data were then reconstructed with 50%, 25% and 10% sparse sampling CT, compared against simulated 50%, 25% and 10% of the original used

Table 3.3.: Radation dose, SNR and CNR of the image under different dose.

	Exposure	CTDI	SNR	CNR
Original	109	7.5	32.8	13.7
50% SpS	55	3.8	21.5	8.7
25% SpS	27	1.9	16.2	6.3
10% SpS	11	0.8	14.2	5.6
50% TC	55	3.8	18.6	7.2
25% TC	27	1.9	9.5	3.8
10% TC	11	0.8	2.9	1.1

SpS indicates sparse sampling. TC indicates tube current (reduction). Exposure is the mean exposure (mAs) of all subjects. CTDI is the mean volumetric CT dose index (mGy) for all subjects. This table was published in J-I.

tube current. Sparse sampling scheme is regularly sampling every 2, 4 and 10 projection data. A simulation tool was used to generate lower tube current scans. The simulation algorithm was based on respective raw projection data [45]. System parameters of the scanner, for example detector gain, were considered in order to account for electronic noise. Therefore, the result was accurate especially under ultra-low tube current conditions [46].

Average of the original dose was 100 mAs (about 7.5 mGy) and the original scans were already relatively low-dose scans. Consequently 50%, 25% and 10% of sparse sampling or tube current simulations were 55, 27 and 11 mAs and can be considered as ultra-low dose in clinical routine, Table 3.3.

Because this study is focused on the trabecular microstructure inside the vertebrae, the image slices were reconstructed with very high resolutions, as 1152 by 1152 pixels with a field of view of 450 by 450 mm^2. SIR stopped at a manually given number of iterations. Original dose SIR reconstructed images are shown in Figure 3.3. Reduced dose images are shown in Figure 3.4 and 3.5.

Bone mineral density (BMD) at the spine of each patient was evaluated inside non-fractured thoracic and lumbar vertebrae, and calibrated with a reference phantom (Mindways Osteoporosis Phantom, Austin TX, USA). The phantom consisted of five rods of basic materials with known equivalent water and dipotassium phosphate (K_2HPO_4) concentrations. Calibrating coefficients were calculated in a least-squares manner with all five rods and for each subject independently [47]. A

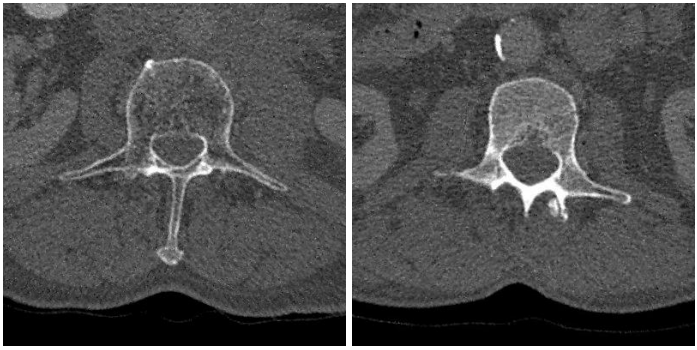

(a) original dose, patient **(b)** original dose, control

Figure 3.3.: SIR image of subjects with (left) and without (right) osteoporotic fracture, original dose.

Patient with osteoporotic fractures has significantly less trabecular structures inside the vertebra compared to the vertebra from (healthy) control subjects. These images were published in J-I

conversion equation was used to empirically eliminate the effect of contrast agent [48].

Trabecular bone microstructure was analyzed [49] [50]. Voxels inside the central vertebra were binarized to be either bone or marrow, with a threshold chosen as 200 mg/cm^3 which was optimized visually for the microstructure analysis. Four morphometric parameters were delivered: bone fraction (BF), trabecular number (TbN, mm-1), trabecular separation (TbSp, mm) and trabecular thickness (TbTh, mm). Parameters were apparent values because the actual CT has limited resolution for these parameters. One texture parameter, fractal dimension (FD), was estimated using a box counting algorithm [51].

To evaluate the extracted parameters, statistical analysis was performed. Paired t-test was used for all tests and a two-sided 0.05 level was considered significant.

No significant change in BMD was observed when analyzing the reduced projections even at 10% sampling rate ($p > 0.05$), whereas lowering tube current to 10% resulted in average 38% higher BMD values, Figure 3.7. For all trabecular parameters, both sparse sampling and lowering tube current affected the mea-

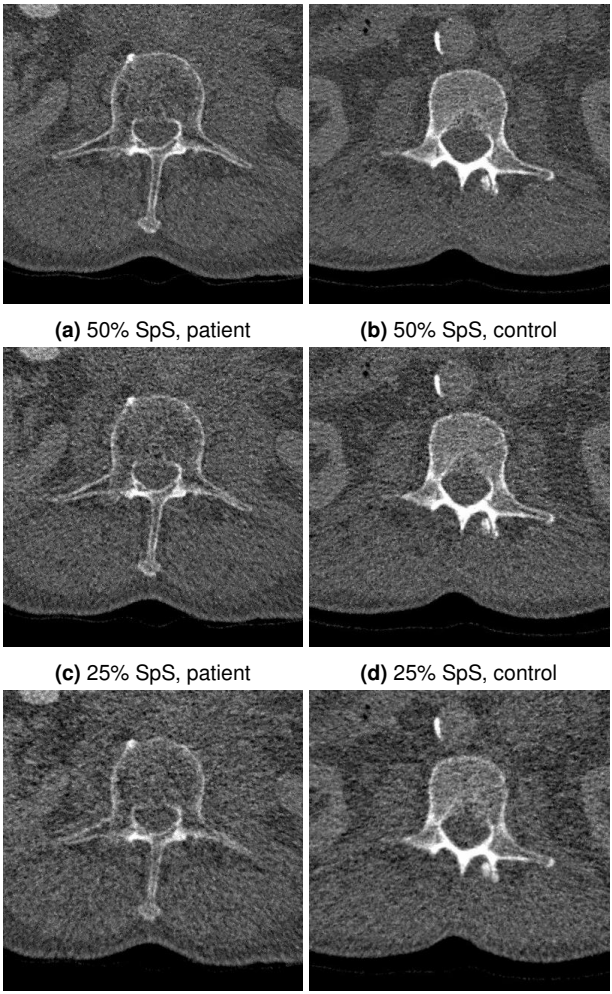

(a) 50% SpS, patient **(b)** 50% SpS, control

(c) 25% SpS, patient **(d)** 25% SpS, control

(e) 10% SpS, patient **(f)** 10% SpS, control

Figure 3.4.: SIR image of subjects with (left, patient) and without (right, control) osteoporotic fracture, 50%, 25% and 10% sparse sampling (SpS).

SpS refers to sparse sampling. Sparse sampling deteriorates general image quality as the sampling rate is reduced.

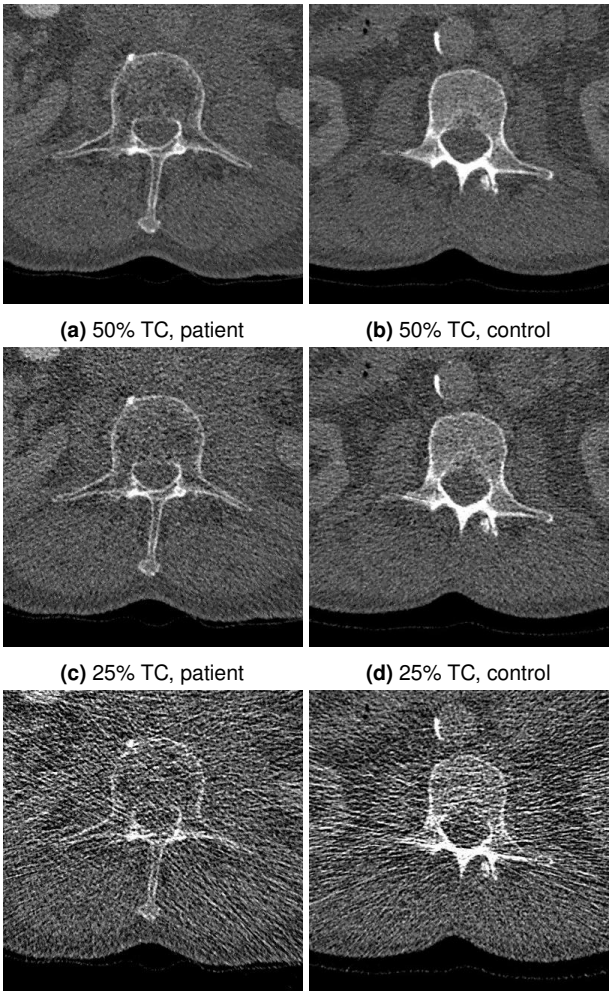

(a) 50% TC, patient **(b)** 50% TC, control

(c) 25% TC, patient **(d)** 25% TC, control

(e) 10% TC, patient **(f)** 10% TC, control

Figure 3.5.: SIR image of subjects with (left, patient) and without (right, control) osteoporotic fracture, 50%, 25% and 10% tube current simulation.

TC represents (reduced) tube current. Reducing tube current creates significant streaking artifacts as the dose is reduced.

surements in various degrees. BF, TbN, FD tended to increase when dose was lowered, while TbSp and TbTh decreased. TbN and TbSp were most sensitive to the dose reduction ($p < 0.001$), around changes of 20% to 40%, Figure 3.9 3.10. All the parameters are illustrated in Figure 3.6, 3.7, 3.8, 3.9, 3.10, 3.11 and 3.12.

For BMD, BF and TbTh, subjects without osteoporotic fractures still had greater values as compared to the matched subjects with osteoporotic fractures in both dose reducing approaches. The two groups could still be differentiated, as differences were statistically significant ($p < 0.05$) even at 10% of the original dose level. For TbSp and FD, the differences between the two groups were significant only when the original dose was used, but was neither significant when data was sparsely sampled nor when tube current was reduced ($p > 0.05$). The difference of TbN between the two groups was not significant at any dose level.

Additional studies were made using the same reconstruction scheme but focused on bone strength based on finite element (FE) analysis (**journal publication J-2 and J-8**).

When lowering tube current, FE-predicted failure load of the standard dose did not significantly differ from the 50% ($p = 0.718$ and $p = 0.670$) and 25% doses ($p = 0.606$ and $p = 0.592$); however, it significantly differed from the 10% dose ($p = 0.00198$ and $p = 0.0354$). In evaluating the differences at each dose, the failure load differed significantly between fracture and control groups at original ($p = 0.0373$), 50% ($p = 0.0305$), and 25% doses ($p = .0233$) but not at 10% dose ($p = 0.458$).

While with the original dose it was possible to differentiate patients with and without fractures (AUC $= 0.675$, $p = 0.0266$), as well as with 50% dose (AUC $= 0.686$, $p = 0.0188$) and 25% dose (AUC $= 0.691$, $p = 0.0137$), however, with 10% dose it was not possible to differentiate between the two patient groups (AUC $= 0.562$, $p = 0.461$). In the pairwise comparison of ROC curves, there were no significant differences between areas of the 50% and 25% doses, compared to the full dose.

As a brief conclusion, ultra-low-dose assessment of osteoporosis related bone attributes (BMD, trabecular microstructure and failure load) may be feasible. Sparse sampling showed great advantage as the BMD did not change when the total effective dose was reduced. The result of apparent trabecular attributes in ultra-low-dose circumstances were less reliable compared to BMD because they were very sensitive to the effective dose, considering both sparse sampling and reducing

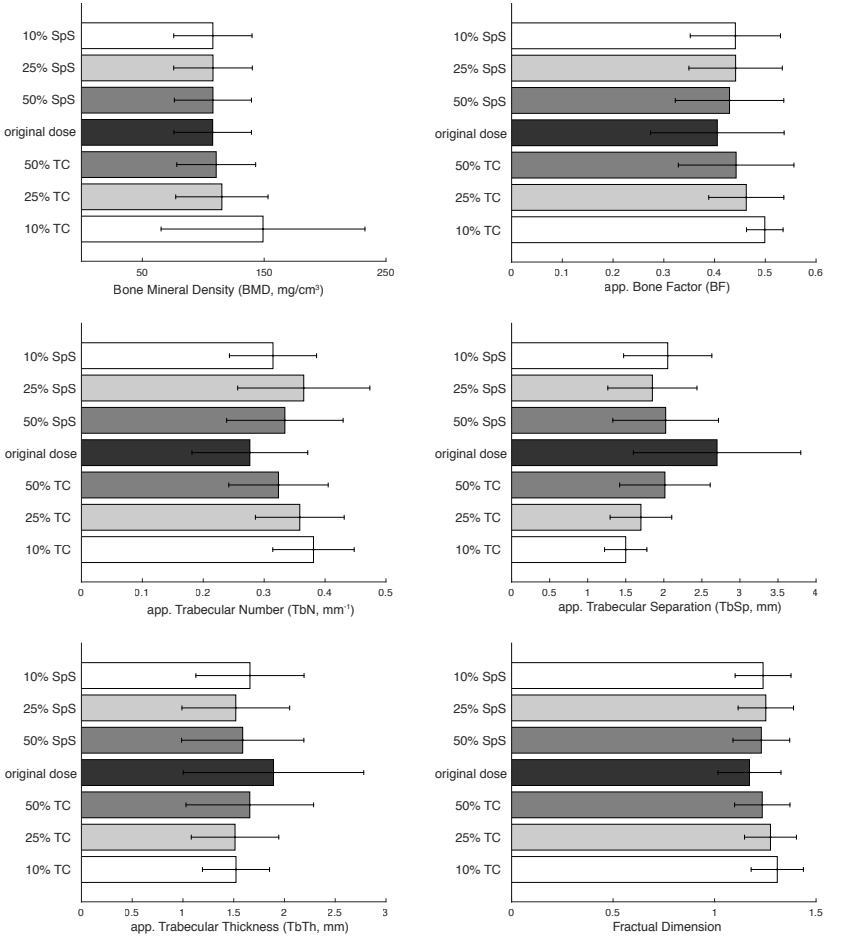

Figure 3.6.: BMD and trabecular parameters extracted with different dose levels.

SpS stands for sparse sampling, TC stands for tube current (reduction). Some of these images were published in J-I.

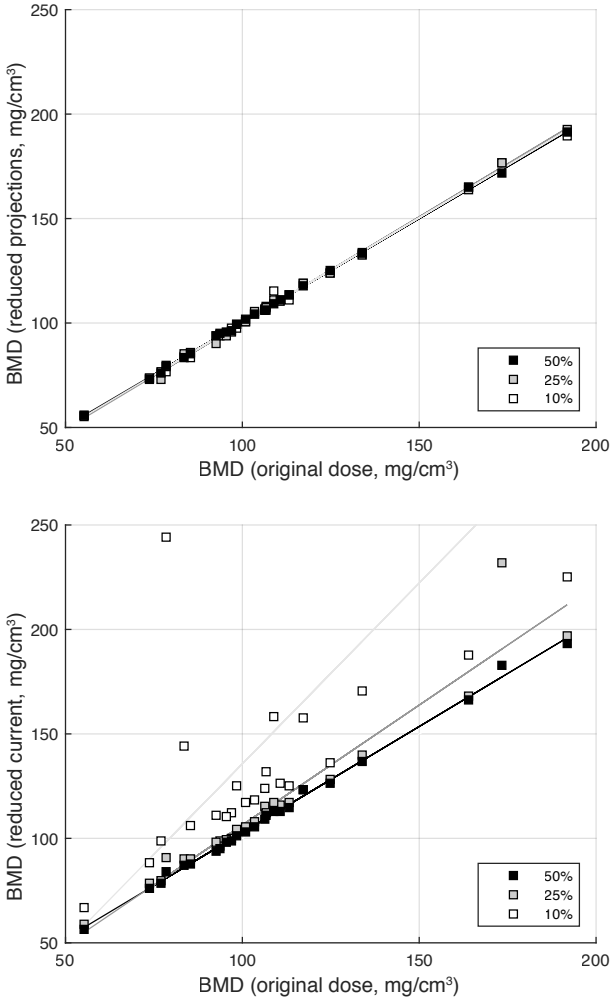

Figure 3.7.: BMD at ultra-low dose compared against original dose.

Top: sparse sampling. Lower: tube current reduction.These images were published in J-I.

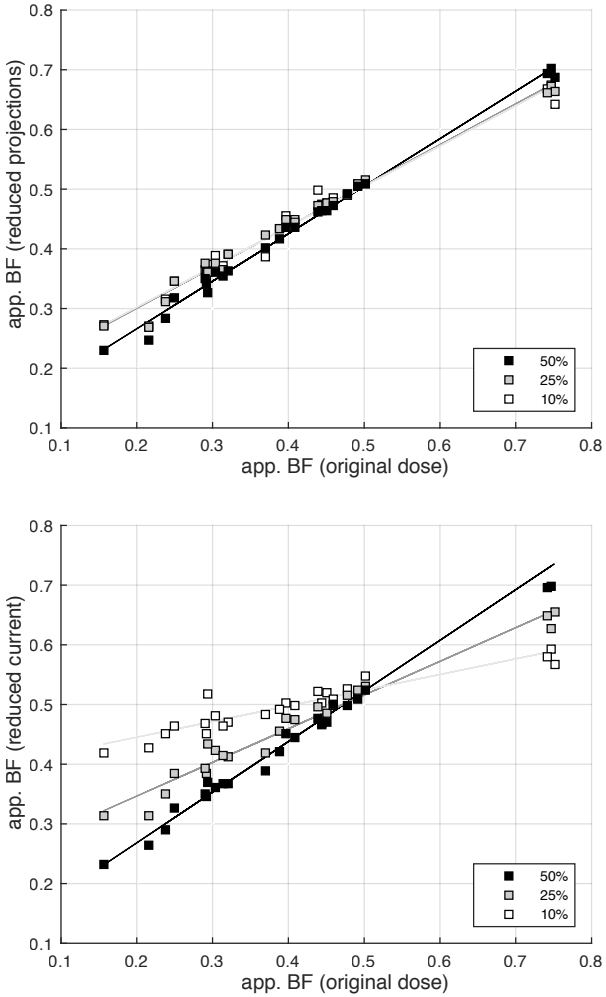

Figure 3.8.: Apparent bone factor (app. BF) at ultra-low dose compared against original dose.

Top: sparse sampling. Lower: tube current reduction. These images were submitted as supplemented material for J-I.

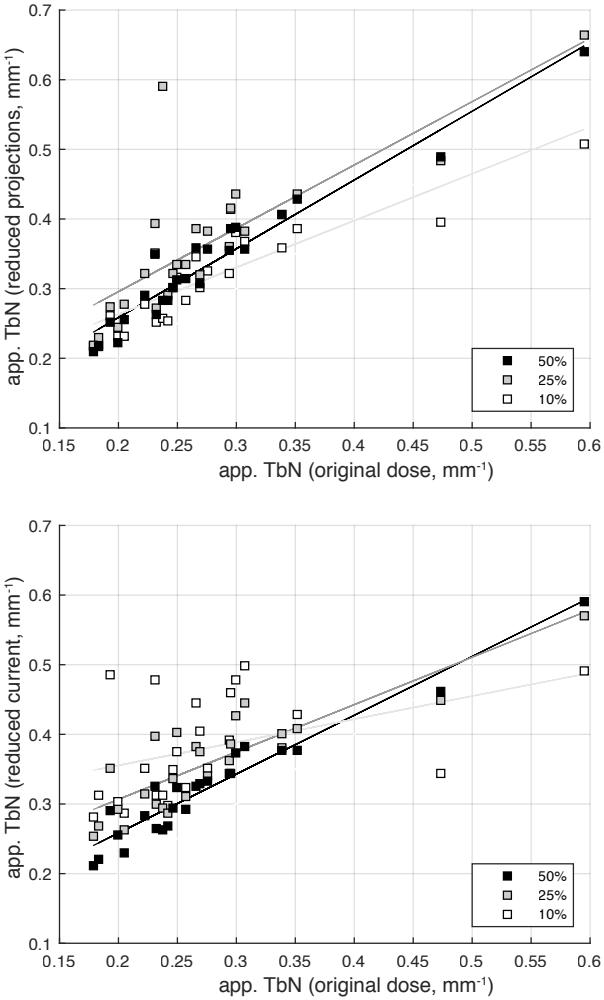

Figure 3.9.: Apparent trabecular number (App. TbN) at ultra-low dose compared against original dose.

Top: sparse sampling. Lower: tube current reduction. These images were submitted as supplemented material for J-I.

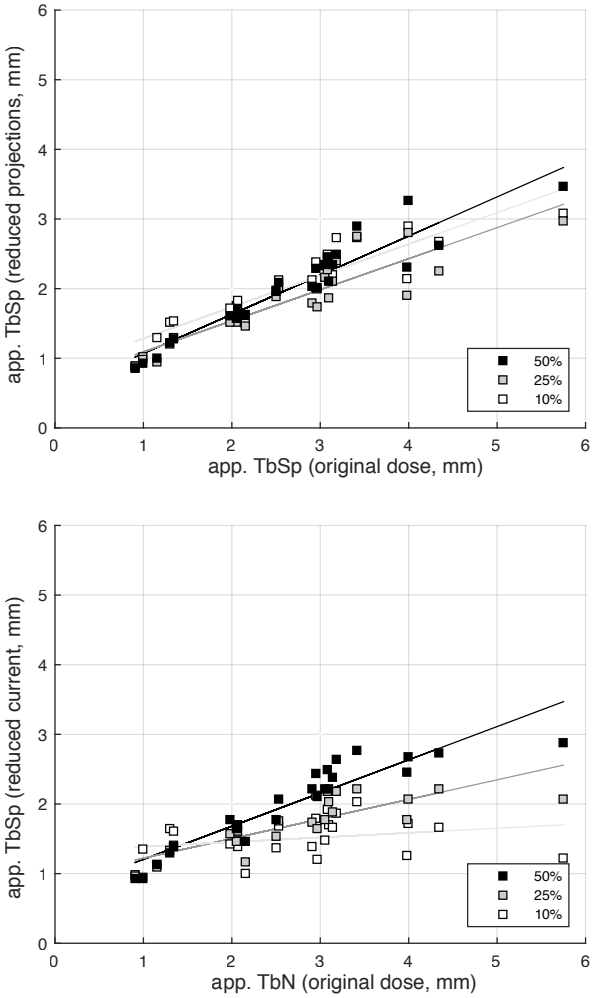

Figure 3.10.: Apparent trabecular separation (App. TbSp) at ultra-low dose compared agains original dose.

Top: sparse sampling. Lower: tube current reduction. These images were submitted as supplemented material for J-I.

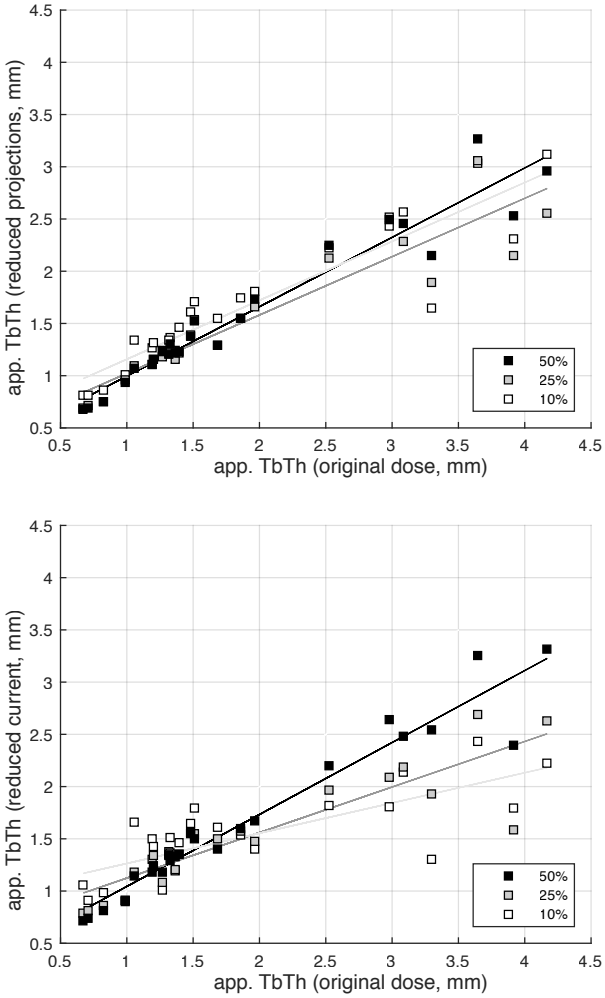

Figure 3.11.: Apparent trabecular thickness (App. TbTh) at ultra-low dose compared agains original dose.

Top: sparse sampling. Lower: tube current reduction. These images were submitted as supplemented material for J-I.

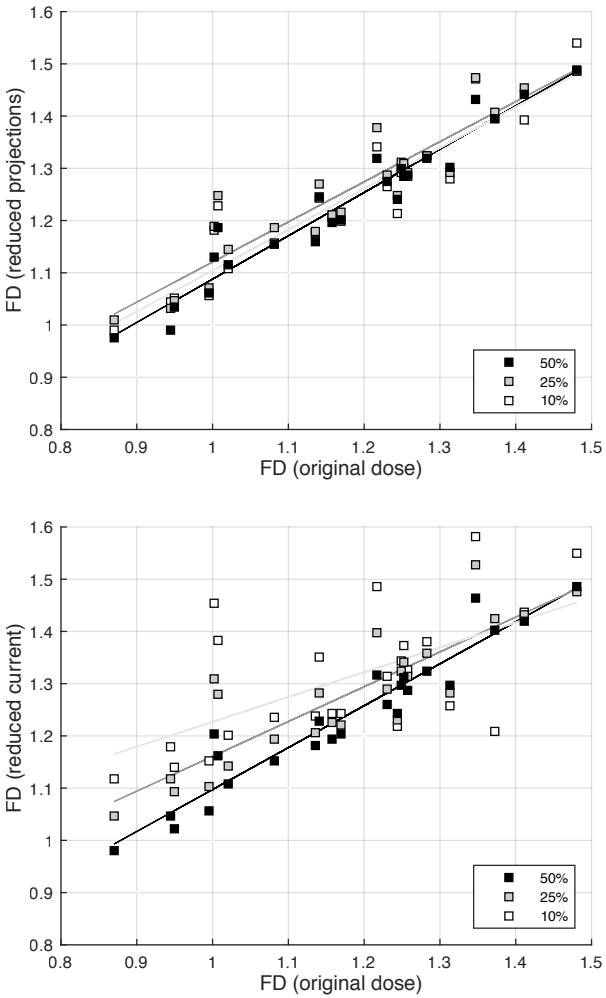

Figure 3.12.: Fractal dimension (FD) at ultra-low dose compared agains original dose.

Top: sparse sampling. Lower: tube current reduction. These images were submitted as supplemented material for J-I.

tube current.

3.3.2. Fracture identification on the spine

A second study was performed to investigate if the radiologist can perceive the fractured site on the spine under ultra-low dose CT with the help of sparse sampling (**journal publication J-12**).

35 subjects were retrospectively included (80% female with average age: 70.6 ± 14.2). 23 subjects (65.7%) had at least one vertebral fracture (patient group) and the other 12 patients showed no vertebral fracture (control group). All included subjects diagnosed with vertebral fractures also underwent MRI scans before or after CT. The original dose information is listed in Table 3.4. These fractures in the patient group affected the cervical spine in 10.0%, the thoracic spine in 40.0%, and the lumbar spine in 50.0%. Based on original CT and MRI scanning, fractures were diagnosed as acute in 58.3% and old in 41.7%.

Table 3.4.: Dose and protocols of the spine fracture patient.

Name	Parameters
Rotation time	1 s (62.9% of subjects), 0.75 s (37.1% of subjects)
Pitch	0.608 (62.9% of subjects), 0.953 (37.1% of subjects)
Tube voltage	120 kV
Tube current	143.4 ± 76.0 mA (49.2 – 326.6 mA)
Exposure	180.4 ± 87.7 mAs (68.0 – 459.0 mAs)
CTDI	11.7 ± 5.7 mGy (4.4 – 29.7 mGy)

This table was published in J-12.

The sparse sampling and tube current reduction simulation schemes were the same as described in previous section at 50%, 25% and 10% of the original dose. SIR was performed with voxel spacing of $0.39 \times 0.39 \times 0.30$ mm^3 in three dimensions (axial slices field of view 200 mm).

A survey was made with two radiologists (6 and 8 years of experience in radiology), who evaluated all imaging data (total 245 datasets) under a clinical diagnosis environment (IntelliSpace Portal version 9.0, Philips Healthcare, Best, the Nether-

Table 3.5.: Diagnostic confidence

	Original dose	50% tube current	50% sparse sampling	p-value
Reader 1	1.02 ± 0.14	1.17 ± 0.38	1.13 ± 0.39	0.48
Reader 2	1.02 ± 0.14	1.15 ± 0.36	1.10 ± 0.31	0.41
		25% tube current	25% sparse sampling	p-value
Reader 1		1.83 ± 0.79	1.34 ± 0.48	< 0.001
Reader 2		1.80 ± 0.79	1.29 ± 0.46	< 0.001
		10% tube current	10% sparse sampling	p-value
Reader 1		2.55 ± 0.69	1.87 ± 0.58	< 0.001
Reader 2		2.45 ± 0.71	1.80 ± 0.51	< 0.001

1 - High confidence, 2 - Medium confidence, 3 - Low confidence.
This table was published in J-12.

lands), provided with axial and sagittal slices with standard bone window (width: 2500 HU, center: 500 HU) and soft-tissue window (width: 360 HU, center: 60 HU). During the evaluation, the number of fractures per subject was determined. Readers also scored the image quality and provided a confidence number of their diagnosis.

Both readers correctly identified all patients of the control group without any assignments of vertebral fractures. For the patients of the fracture group, a total of 48 vertebral fractures were observed with 100% dose and projections, Table. 3.6.

Both virtual tube current reduction and sparse sampling led to decreased overall image quality, increased overall artifacts, and reduced contrast of vertebrae according to the evaluation of both readers. When comparing virtually lowered tube current to sparsely sampled data-sets for overall image quality, sparse sampling resulted in significantly better confidence according to each reader for all comparisons, Table 3.5.

Virtual tube current reduction with 50% of the original current allowed for correct detection of all vertebral fractures (Reader 1) and 95.8% (Reader 2) of vertebral fractures when compared to original dose images. Further lowering to 10% resulted to correct detection of 79.2% (Reader 1) and 87.5% (Reader 2) of vertebral fractures. 50% sparse sampling images allowed for the correct detection of all

Table 3.6.: Reported number of fractures

	Original dose	50% tube current	50% sparse sampling
Reader 1	48	48	48
Reader 2	48	46	48
		25% tube current	25% sparse sampling
Reader 1		47	47
Reader 2		45	45
		10% tube current	10% sparse sampling
Reader 1		38	46
Reader 2		42	44

This table was published in J-12.

Table 3.7.: Status of fracture (acute/unclear/old)

	Original dose	50% tube current	50% sparse sampling	κ
Reader 1	28/0/20	27/2/19	27/1/20	0.84
Reader 2	28/0/20	27/3/16	26/1/21	0.79
		25% tube current	25% sparse sampling	κ
Reader 1		18/20/9	26/2/19	0.42
Reader 2		18/22/7	25/3/17	0.35
		10% tube current	10% sparse sampling	κ
Reader 1		4/30/4	16/24/6	0.24
Reader 2		4/34/4	15/24/5	0.13

This table was published in J-12.

vertebral fractures by both readers. Further decreasing the number of projections down to 10% of the original data allowed for correct detection of 95.8% (Reader 1) and 91.7% (Reader 2) of vertebral fractures (Table 3.6).

Concerning the age of reported fractures, sparse sampling also showed better results regarding the differentiation between acute, old, and unclear fracture ages, Table 3.7. For 25% sparse sampling images, the fracture age was determined as unclear in 4.3% (Reader 1) and 6.7% (Reader 2) of detected vertebral fractures.

As a summary, the assessment of bone fractures with ultra-low-dose scans is feasible. The scheme of combining sparse sampling and SIR showed better accuracy than reducing the tube current.

3.3.3. Bone mineral density on the femur site

Human femur is also one important site regarding the diagnosis of osteoporosis. It is where DXA is applied to evaluate the bone mineral density. A study was performed on the femoral site (**journal publication J-11**).

41 subjects (34% female with average age: 69.3 ± 10.1) were included. The field of view of the scans covered the proximal femur of both sides down to the minor trochanter in all subjects. Similar to the previous studies, the simulation algorithm generated lower tube current reconstructions based on raw projection data at 50%, 25% and 10% of the original tube current and sparse sampling was applied at levels of 50%, 25% and 10%. Both FBP and SIR reconstructions were used in this study.

FBP and SIR based-mean BMD values derived from original dose are 849 mg/cm^3 for FBP and 864 mg/cm^3 for SIR. Lowering the tube current down to 10% changed the BMD up to 1125 mg/cm^3 for 10% dose FBP and 1130 mg/cm^3 for SIR, which are roughly 32.5% increase. With sparse sampling, BMD measurement remained comparatively stable, with 853 mg/cm^3 for FBP and 860 mg/cm^3 for SIR.

3.4. Discussion

This chapter investigated sparse sampling and model-based statistical iterative reconstruction as novel data acquisition and reconstruction scheme to perform ultra-low-dose musculoskeletal CT imaging. It showed that fracture risk assessment is feasible.

The main limitation of this method is that sparse sampling CT is not available for current clinical CT because extra units need to be added to the X-ray source generator. This thesis only discusses the possible outcome of the images but whether or not these extra units are fast enough to switch on and off the X-ray source without introducing other problems must be further evaluated and tested.

SIR used in this thesis is developed for academic purposes and needs large memory and heavy computation to generate patient images. The long computation time is clinically unacceptable for routine CT examinations but can be reduced if the parallel computing hardware and algorithms are further optimized. In addition, optimized reconstruction parameters in SIR are also essential for specific CT protocols and patient size. This specific parameterization including the strength of regularization, number of iterations, etc. could be difficult to evaluate in real situations and needs to be further investigated and evaluated.

4. Multi-energy computed tomography

Multi-energy CT offers some of the most advanced clinical applications in modern CT. This chapter summarizes the research during this PhD project involving dual-layer based multi-energy CT.

The first section briefly introduces the physics' background of multi-energy CT. The second and third section summarize two major research topics of multi-energy CT: material quantification and material decomposition.

4.1. Physics of multi-energy computed tomography

In an ideal case of a narrow X-ray beam of monoenergetic photons in the range of clinical CT (E < 150 keV), the attenuation of objects can be attributed to three main physical interaction mechanisms: photoelectric absorption [52], incoherent (Compton) scattering [53] and coherent (Rayleigh) scattering [54].

Photoelectric absorption occurs when a X-ray photon hits an electron in the inner shell, the photon is absorbed and the electron is released. Compton scattering refers to the incident where a photon interacts with an electron in an outer shell, the photon gives a part of its energy to the electron and changes its traveling direction. Rayleigh scattering is a process in which the photon is scattered by an electron and the atom is neither ionized nor excited. The chances of the occurrences of photoelectric absorption or Compton scattering are random but energy dependent. Because Rayleigh scattering mostly happens at low energies and for dense materials, it is often neglected when discussing the attenuation of X-rays for body tissues in medical CT.

If written in an equation, the mass attenuation coefficient of X-rays for an object

following Beer-Lambert's law (Equation 2.2) can be represented by:

$$\frac{\mu(E)}{\rho} \simeq a_p f_p(E) + a_c f_c(E), \tag{4.1}$$

where $\mu(E)/\rho$ is the mass attenuation coefficient (cm^{-1}), a_p and a_c are characteristic parameters of photoelectric absorption and Compton scattering of the material, f_p and f_c are the energy dependencies of photoelectric absorption and Compton scattering.

The photoelectric absorption part can be approximated as:

$$a_p f_p \simeq \rho_e C_p \frac{Z^m}{E^n}, \tag{4.2}$$

where ρ_e is the absolute electron density (e/cm^3), C_p is constant and equals to 9.8$\times$10^{-24} [55], Z is the effective atomic number, the energy of X-ray beam E is measured with the unit keV. For a numerical fit of the experimental data, m is between 3 and 4, and n between 3 and 3.5. This thesis uses m = 3.8, n = 3.2 [56].

Compton scattering can be approximated with electron density and the total Klein-Nishina cross-section [57]:

$$a_c = \rho_e, \tag{4.3}$$

$$f_c(\gamma) = C_0 \left\{ \frac{1+\gamma}{\gamma^2} \left[\frac{2(1+\gamma)}{1+2\gamma} - \frac{1}{\gamma} \ln(1+2\gamma) \right] + \frac{1}{2\gamma} \ln(1+2\gamma) - \frac{1+3\gamma}{(1+2\gamma)^2} \right\}, \tag{4.4}$$

where

$$\gamma = \frac{E}{510.875\ keV}, \tag{4.5}$$

$$C_0 = 2\pi r_0^2. \tag{4.6}$$

The X-ray energy E has the unit of keV. r_0 is the classical electron radius, which is a constant and equals to 2.818$\times$10^{-13} cm.

After summarizing all these equations, we can obtain:

$$\frac{\mu(E)}{\rho} \simeq \rho_e C_p \frac{Z^m}{E^n} + \rho_e f_c(E). \tag{4.7}$$

Because of Z^m/E^n, photoelectric absorption is very prominent and becomes very substantial if the scanned object has a high effective atomic number Z (such

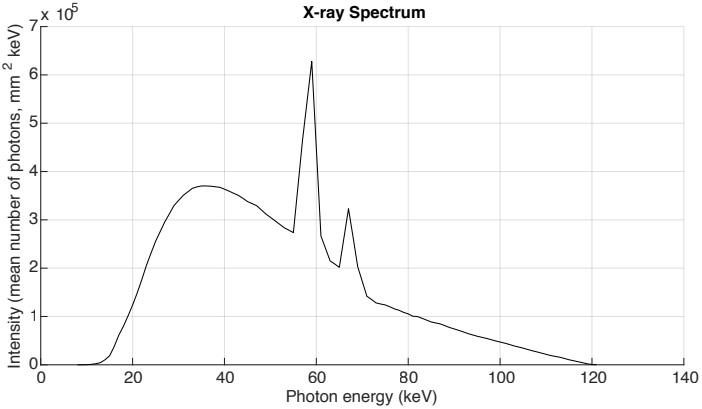

Figure 4.1.: X-ray spectrum

Tungsten anode X-ray spectrum is simulated with 120 kV peak tube voltage [59] [60]. The generated spectrum has mean energy of 51.52 keV. This data is online available [61].

as metals and medical implants) and the X-ray energy E is low. Compared to photoelectric absorption, Compton scattering is less varying with Z and E. As a result, dense materials appear much brighter and the contrast is much higher in lower energy CT images, compared to CT scans using higher energy X-ray.

In a conventional medical CT, the X-ray is a broad spectrum light (polychromatic beam), Figure 4.1 [58]. The signal g received at the detector can be seen as a summation of monochromatic X-ray beams, represented by the integral of attenuation occurrences in all energies:

$$g = \ln \int_0^{\max} S(E) \exp\left(-\frac{\mu(E)}{\rho}\right) dE, \tag{4.8}$$

where $S(E)$ stands for the X-ray intensity at energy E emitted at the source.

Multi-energy CT stands for techniques which can selectively capture X-ray signal in specific and separate ranges. For example, a dual-source based CT has two X-ray sources and can thus scan the object with X-rays of two different spectra. One source can have high peak kilovoltage power while the other source has low peak kilovoltage. A dual-layer based CT is equipped with a special detector. The

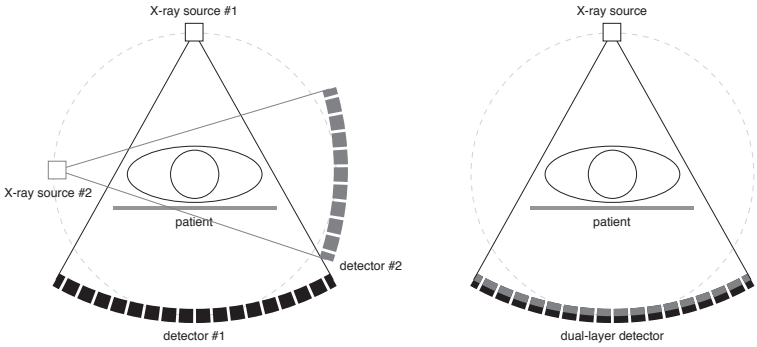

(a) Dual-source CT **(b)** Dual-layer CT

Figure 4.2.: Dual-energy CT Systems.

4.2a: In dual-source based system, there are two X-ray sources and two detectors perpendicular to each other. 4.2b: In dual-layer based system, a special detector is used to record high and low energy photons separately.

detector's first layer primarily records X-ray photons with lower energy and the other layer higher energy photons, Figure 4.2.

In such dual-energy systems, the scanner obtains two signals:

$$g_L = \ln \int_{L_1}^{L_2} S_L(E) \exp\left(-\frac{\mu(E)}{\rho}\right) dE, \tag{4.9}$$

$$g_H = \ln \int_{H_1}^{H_2} S_H(E) \exp\left(-\frac{\mu(E)}{\rho}\right) dE, \tag{4.10}$$

where L_1 and L_2 are the spectrum boundaries of the low energy X-ray and H_1 and H_2 the higher energy X-ray.

By combining these two signals, virtual monoenergetic images can be synthesized [62]. A virtual monoenergetic image represents the attenuation as if the X-ray beam has a single particular energy (monochromatic beam) and the energy does not change during the X-ray and atom interaction. Thus, the information contained in a virtual monoenergetic image at energy E is then regarded as the summation of photoelectric absorption and Compton scattering only at E.

$$g(E) = \frac{\mu(E)}{\rho} = \rho_e C_p \frac{Z^m}{E^n} + \rho_e f_c(E). \tag{4.11}$$

Of note, virtual monoenergetic images are not real monoenergetic images, while monoenergetic images can only be generated with monochromatic X-ray beam, such as synchrotron X-rays, and cannot neglect the photon energy changes during the Compton scattering. In the rest of this thesis, monoenergetic images are referred to virtual monoenergetic images.

Journal publication J-III discussed one of the clinical applications of virtual monoenergetic images, determining relative electron density of the human body, which is an important procedure during radiation therapy planning. In that paper, two methods of measuring relative electron density with virtual monoenergetic images (the theoretical model using equation 4.7 and an empirical calibrating method [63] [64])) were studied with Gammex phantom (467-TOMO, Gammex RMI, Middleton WI, USA) and Catphan phantom (Catphan 504, the Phantom Laboratory, Salem NY, USA). The average error of determining electron densities in dual-layer CT is between 0.87% and 1.53%.

The following sections discuss more applications of monoenergetic images (materials quantification and decomposition) based on specific clinical musculoskeletal interests.

4.2. Material quantification

In monoenergetic images at lower energies, contrast is much higher due to a higher contribution of photoelectric absorption. By quantifying the differences between high and low energy monoenergetic images, it is possible to make quantitative measurements of dense material in the multi-energy CT scan, such as to determine bone mineral density (BMD).

4.2.1. Calcium quantification for ex-vivo specimens

A pilot study on quantifying BMD for ex-vivo human vertebral specimens was performed and published in detail in **journal publication J-II**. If the composition of a material is known, for example, a mixture of calcium and water/water-like substances, the fraction of calcium (or any denser substance with a varying X-ray absorption depending on the energy of the photons) can be estimated with two

monoenergetic images with two distinguishable keV.

Assuming volume conservation and that the subject is a mixture containing calcium and non-calcium components (hydrogen, oxygen, carbon, etc.). The attenuation coefficients of the mixture at 50 and 200 keV monoenergetic CT images can be summarized in the following equations:

$$\frac{\mu_{50}}{\rho} = f_{Ca}\frac{\mu_{Ca,50}}{\rho_{Ca}} + f_n\frac{\mu_{n,50}}{\rho_n}, \tag{4.12}$$

$$\frac{\mu_{200}}{\rho} = f_{Ca}\frac{\mu_{Ca,200}}{\rho_{Ca}} + f_n\frac{\mu_{n,200}}{\rho_n}, \tag{4.13}$$

where μ_{50}/ρ is the mass attenuation coefficient of the mixture at 50 keV, f_{Ca} is the fraction of calcium component, $\mu_{Ca,50}/\rho_{Ca}$ is the mass attenuation coefficient of calcium component. f_n and $\mu_{n,50}/\rho_n$ the corresponding non-calcium component.

Because X-ray attenuation of the mixture linearly increases with the calcium concentration, the Hounsfield unit (HU) of the mixture in both 50 keV and 200 keV images should proportionally increase as the calcium fraction increases. This phenomenon is depicted with a solid line in Figure 4.3. The four point clouds represent four calcium hydroxyapatite (HA) phantom with 100, 209, 405 and 809 mg/cm^3 concentration. The black solid regression line from these points represents the behavior of calcium in 50 and 200 keV monoenergetic images. It is different to the diagonal dashed line and tilts to the 50 keV axis, because at 50 keV calcium attenuates X-rays much more than at 200 keV.

Derived from Equation 4.12, this regression line can be represented as:

$$(\frac{\mu_{200}}{\rho} - f_n\frac{\mu_{n,200}}{\rho_n}) = \frac{\mu_{Ca,200}}{\mu_{Ca,50}}(\frac{\mu_{50}}{\rho} - f_n\frac{\mu_{n,50}}{\rho_n}). \tag{4.14}$$

The slope of this line μ_{200}/μ_{50} is a known constant and can be computed by values looked up from database, for example, the United States National Institute of Standards and Technology (NIST) X-Ray Mass Attenuation Coefficients Database. This slope is free from the influences of radiation dose and the calcium concentration.

In cases that the non-calcium component is pure water or if we can ignore the difference of the amount of X-ray absorbed from the non-calcium component at both 50 and 200 keV, $\mu_{n,50}$ equals to $\mu_{n,200}$. The fraction of calcium can be simply estimated by:

$$f_{Ca} = \frac{\rho_{Ca}}{\rho} \cdot \frac{\mu_{50} - \mu_{200}}{\mu_{Ca,50} - \mu_{Ca,200}}. \tag{4.15}$$

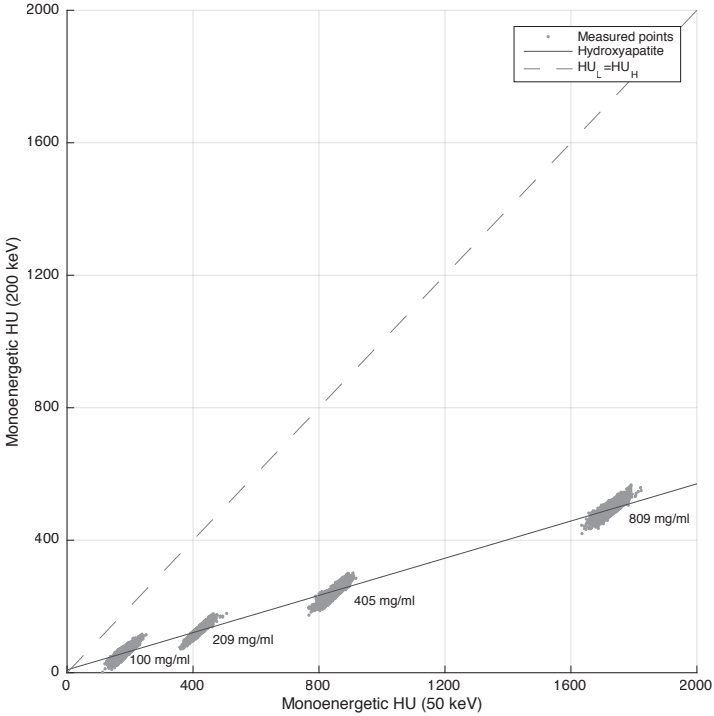

Figure 4.3.: Hydroxyapatite phantoms in monoenergetic 50 and 200 keV.

Monoenergetic Hounsfield units at 50 (x-axis) and 200 (y-axis) keV of four hydroxyapatite phantoms with known concentrations (100, 209, 405 and 809 mg/ml). The black solid line is the regression line of these points. The dashed line is the diagonal line indicating HU in 50 keV equals in 200 keV. This image was published in J-II.

In order to determine the slope of Equation 4.14, four cylindrical phantoms mentioned above were scanned at high radiation dose (120 kVp, 1000 mAs) in a dual-layer CT (iQon, Philips Healthcare, Best, the Netherlands), where an anthropomorphic phantom (QRM, Möhrendorf, Germany) was used to simulate an actual human body, Figure 4.4.

Two monoenergetic images were generated at 50 and 200 keV with Intellispace Portal (Philips Healthcare, Best, the Netherlands). The intensities (in HU) of the

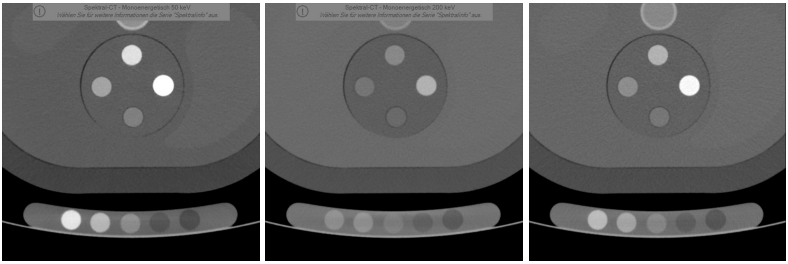

(a) 50 keV **(b)** 200 keV **(c)** conventional image

Figure 4.4.: Hydroxyapatite phantoms in dual-energy CT

Left: monoenergetic CT image at 50 keV. Center: monoenergetic CT image at 200 keV. Right: conventional CT image. HA has higher intensity in monoenergetic images with low ke. These images were published in J-II.

phantoms were measured in regions of interest (ROI), which were cylinders with diameter of 5 mm and height of 33 mm located in the center of the four phantoms.

A line function depicting the relationship with two monoenergetic HA HUs can then be fitted to mimic Equation 4.14:

$$\mathrm{HU}_L = a \cdot \mathrm{HU}_H + b. \tag{4.16}$$

HU_L and HU_H are HUs of HA phantoms measured in monoenergetic 50 and 200 keV images respectively. a is a fitting parameter specific for HA (calcium). b is a fitting parameter adjusting for water. In this set-up, pixels in the ROIs only contain HA and water, therefore pixels in the ROIs (pairs of HU_L and HU_H for HA) are always located along or close to the line described by this equation. A higher distance of the points on the line to the origin reflects a higher HA concentration.

At the same time, HU_L (and also HU_H) is proportional to the exact concentration (mg/cm^3) of HA (BMD):

$$\mathrm{HU}_L = u \cdot \mathrm{BMD} + v. \tag{4.17}$$

Fitting parameters u and v are obtained from known BMD values of the four HA phantoms and the corresponding measured HU_L in the monoenergetic image at 50 keV derived from the calibration scan. u is related by the mass attenuation coefficient of HA at monoenergetic 50 keV. v is related to the CT number determined by water. a, b, u and v are scanner specific variables and can be computed prior to specimen scans.

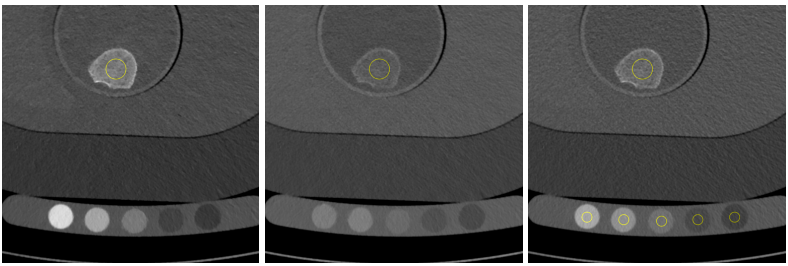

(a) 50 keV **(b)** 200 keV **(c)** conventional image

Figure 4.5.: Vertebral specimen in dual-energy CT

Left: monoenergetic CT image at 50 keV. Center: monoenergetic CT image at 200 keV. Right: conventional CT image. Regions of interest are placed inside the vertebrae and the QCT phantom in order to compute BMD. These images were published in J-II.

Next, the calibration lines from Equation 4.16 and 4.17 can be used to identify and quantify BMD values in multi-energy CT images. 13 mid-vertebral specimens harvested from human donors without history of pathological bone changes other than osteoporosis were examined in this study. Specimens consisted of mid-vertebral, 10-mm-thick axial slices of thoracic vertebrae between T5 and T12. Specimens were preserved in formalin, after complete removal of surrounding soft tissue. Before the scan, specimens were immersed in a water bath and air inside the trabecular bone was eliminated using a vacuum machine. Specimens were then placed in the same anthropomorphic abdomen phantom analogous to their physiologic orientation in the human body, Figure 4.5. Successively, two extension rings simulating fat were placed around the phantom, with the smaller one increasing the diameter to 350 x 250 mm, and the larger one to 400 x 300 mm, simulating patients with waist circumferences 98.5 cm and 114.3 cm, respectively.

Scans were made with 500, 250, 125, 50 and 38 mAs. 250 mAs was considered as standard clinical CT dose. ROIs were placed manually in the center of vertebral specimens. ROIs were 2D circles with diameter of 5.9 mm or 7.8 mm, depending on the vertebra size, and were placed on three slices in the middle of the vertebrae. Measurements of two CT numbers $(\mathrm{HU}'_H, \mathrm{HU}'_L)$ at 50 and 200 keV were extracted from the corresponding monoenergetic images. The distance d from this measurement $(\mathrm{HU}'_H, \mathrm{HU}'_L)$ to the line specified by Equation 4.16 was computed,

Figure 4.6:

$$d = \frac{|a\mathrm{HU}'_H - \mathrm{HU}'_L + b|}{\sqrt{a^2+1}}. \tag{4.18}$$

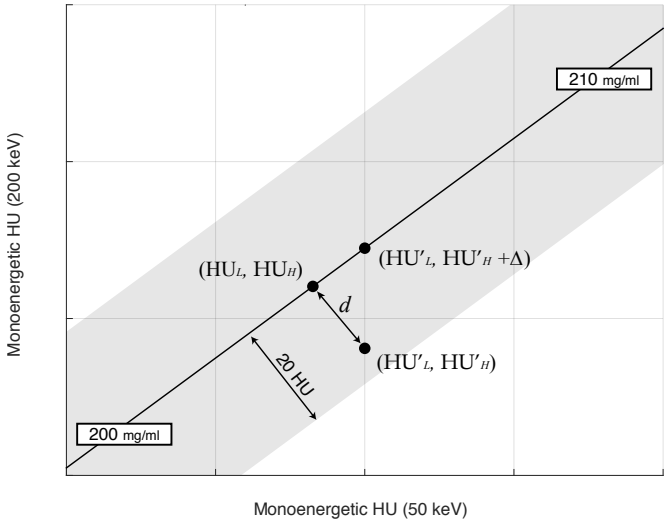

Figure 4.6.: Computing BMD with two monoenergetic HUs.

Measurements (HU'_L, HU'_H) are converted to (HU'_L, HU'_H) for an estimation of BMD using Equation 4.19. A point far away from the line (outside of the gray area) is considered as 'not bone' and is omitted.

A threshold d was applied to identify HA. A measurement was considered bone if it was close to the regression line (d was less than 20 HU). If d was greater than 20 HU, the measurement was likely to represent non-HA material, such as water or soft tissue. For each measurement of (HU'_L, HU'_H) that was considered to represent bone, its BMD value was estimated. In order to minimize possible measurement errors, each measurement was projected to the regression line. For this, the closest point on the line (HU_L, HU_H) to the actual measurement (HU'_L, HU'_H) was determined with the following equation:

$$\mathrm{HU}_L = \frac{\mathrm{HU}'_L + a\mathrm{HU}'_H - ab}{a^2+1}. \tag{4.19}$$

Of note, HU_H can also be determined but is not necessary for generating BMD.

This HU_L was finally converted to a BMD value with the calibrated Equation 4.17. This procedure was performed pixel-by-pixel in a given ROI, and resulting BMDs were averaged.

For comparison purpose, BMD was also calculated with the conventional quantitative CT (QCT Pro Bone Mineral Densitometry Software, Phantom Module. Version 4.0, Mindways, TX, USA). For these scans, a QCT calibration phantom (Mindways) was placed beneath the anthropomorphic phantom. This QCT phantom contains five rods with known density equivalents for phosphate and water.

For each scan, mean values of the five rods in the QCT phantom were measured in the conventional images generated by the dual-layer spectral CT scanner. The ROI selection was similar to the one described in the previous section. Conversion functions for the scanner were computed in a least square manner with MATLAB (MathWorks, Inc. Natick, MA, USA).

The quantification of BMD values with monoenergetic images for known HA phantoms gives satisfactory results. When the radiation exposure was equal or above 250 mAs, absolute BMD difference was less than 5 mg/cm^3 and the relative error was below 3%. At 125 mAs, which is the closest radiation dose level to most clinical low dose CT examinations, the error was smaller than 5% (less than 15 mg/cm^3). However, the accuracy dropped significantly when the dose level was further reduced. At 50 mAs, the relative error was over 14%.

For the vertebral specimen scans, results computed from spectral images were generally lower than the results obtained from conventional QCT, Figure 4.7 and 4.8. The decrease was 6.7 ± 5.7 mg/cm^3 at 500 mAs scans and 8.6 ± 7.6 mg/cm^3 at 125 mAs. Patient size also affects the BMD quantified from monoenergetic images. In relatively lower radiation dose level, multi-energy CT showed higher and more varying BMD values for patients with thicker abdomen size. At 125 mAs, the mean measured BMD for all specimens was 136.2 ± 38.1 mg/cm^3 with larger extension ring (thick torso) and 133.7 ± 32.2 mg/cm^3 with smaller extension ring (thin torso).

BMD result computed from monoenergetic images were compared to the result from QCT approaches. The specimens with higher BMD in QCT consistently showed higher BMD in monoenergetic images. The correlation between the two approaches was strong for all scans with doses above 50 mAs. ($r > 0.97$). Paired-t

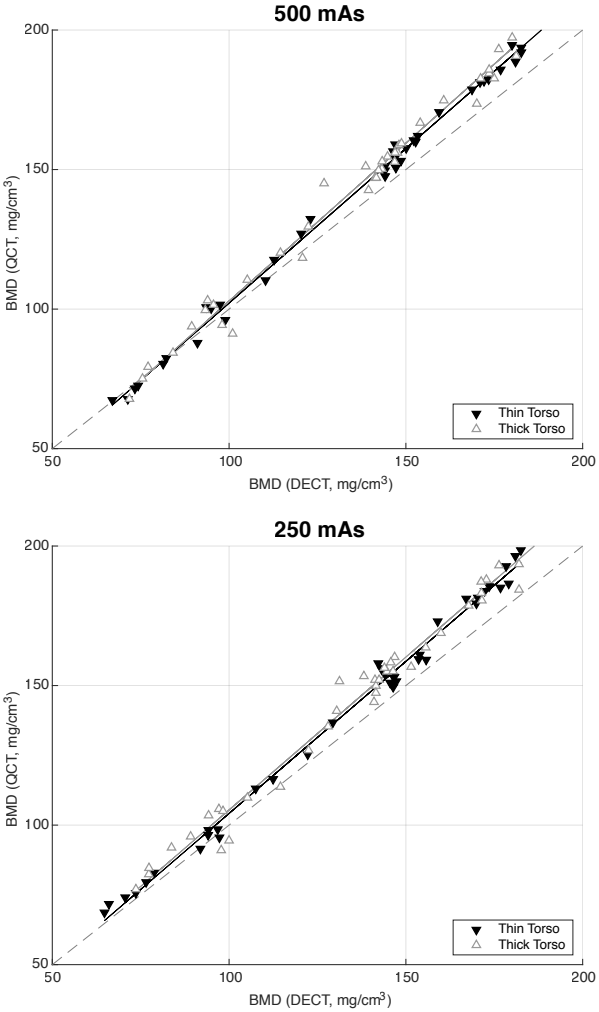

Figure 4.7.: Correlation of BMD values measured in multi-energy CT against QCT (500 and 250 mAs)

These images were published in J-II.

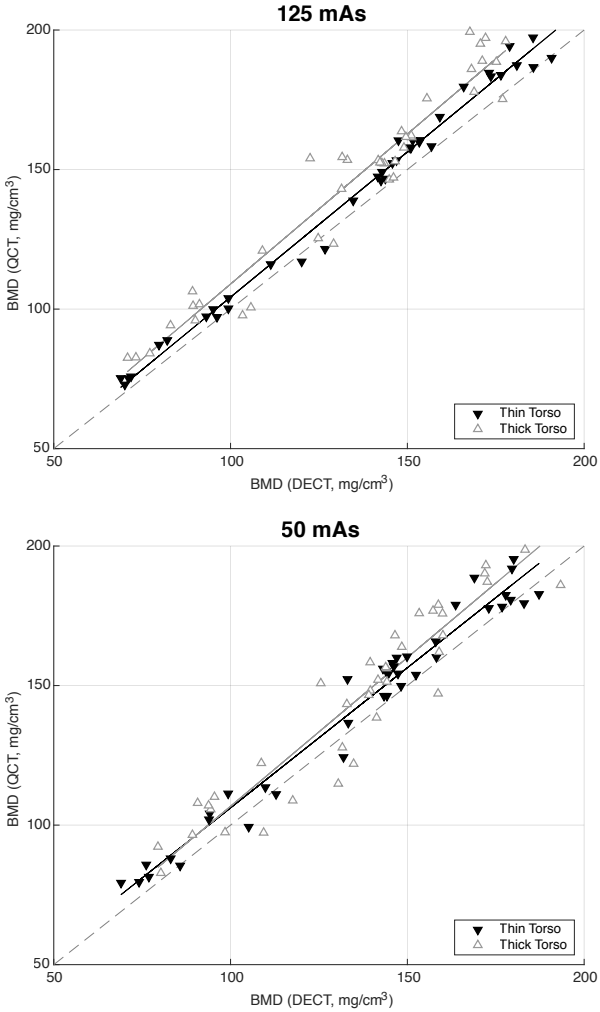

Figure 4.8.: Correlation of BMD values measured in DECT against QCT (125 and 50 mAs).

These images were published in J-II.

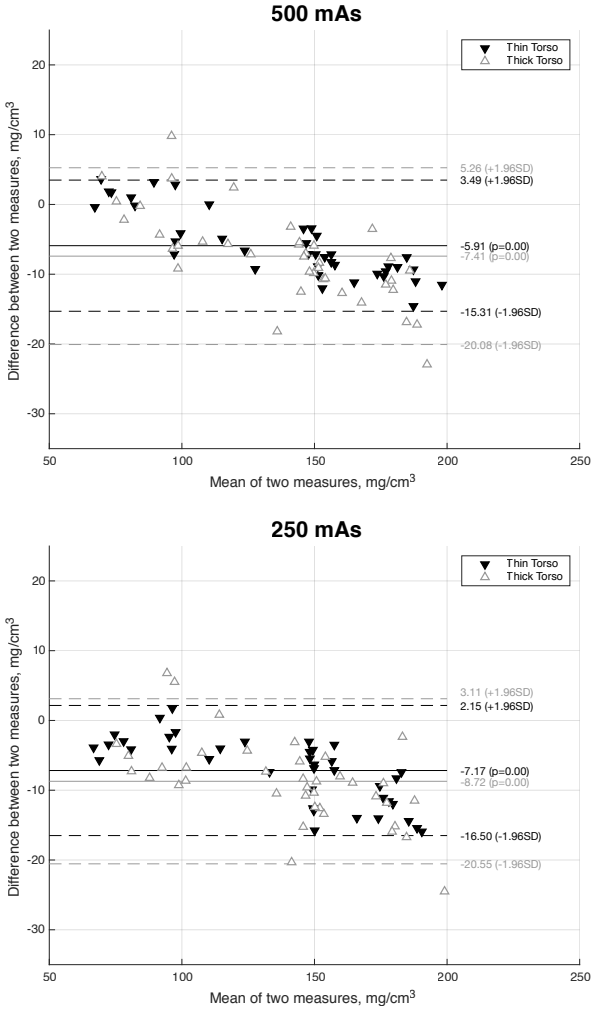

Figure 4.9.: Bland-Altman plot of BMD values measured in DECT and QCT (500 and 250 mAs).

These images were published in J-II.

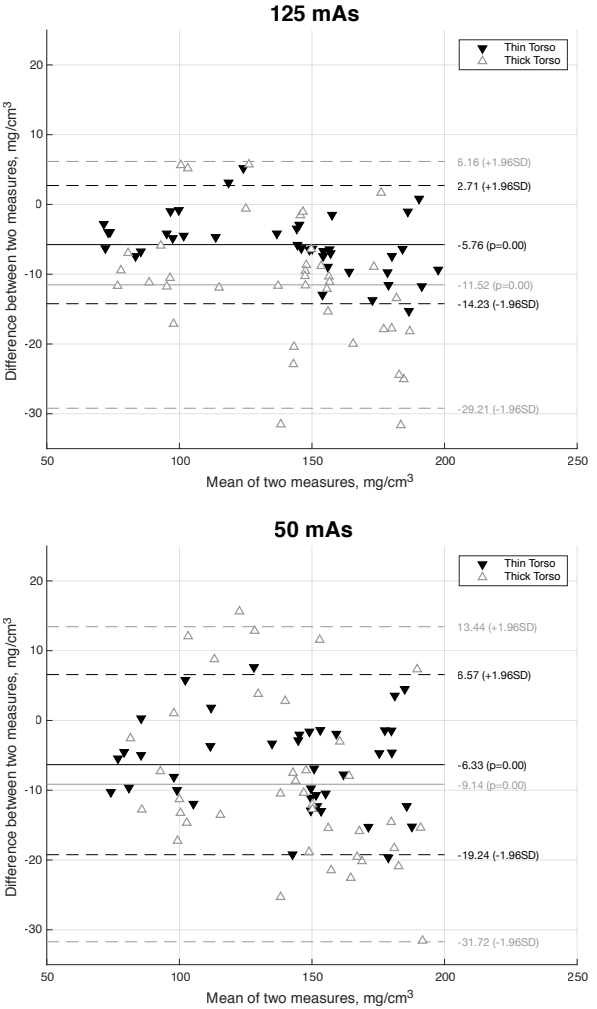

Figure 4.10.: Bland-Altman plot of BMD values measured in DECT and QCT (125 and 50 mAs).

These images were published in J-II.

testand Wilcoxon signed rank test both showed that mid-vertebral specimens were differentiable at all dose levels above 10 mAs. ($p < 0.01$)

In addition, agreement of BMD results between multi-energy CT and QCT was assessed with Bland-Altman plot, Figure 4.9, 4.10. At 50 mAs and above, most differences were between ± 1.96 standard deviation for most cases, indicating a good agreement between both measurements.

4.2.2. Bone mineral density in in-vivo subjects

The study involving in-vivo HA specific BMD measurements was published in **journal publication J-14**. 79 clinical routine scans were collected where patients were undergoing dual-layer CT scans (52% female with average age 66 ± 18). Among them, there were 38% fracture-positive and considered as suffering osteoporosis with low BMD. Similar to the ex-vivo experiment discussed above, in-vivo BMD values obtained from the monoenergetic image method were compared with values from conventional QCT-based measurements.

In the first part of the study with a collection of 33 patients (45% osteoporosis), BMD values derived from monoenergetic images and from QCT were highly correlated ($r = 0.987$, $p < 0.001$). The corresponding Bland-Altman plot shows an excellent agreement between the methods. Area under the ROC curve (AUC) was 0.889 (95% confidence interval [CI]: 0.782-0.996) for QCT-based BMD measurements and 0.878 (95% CI: 0.764-0.991) for monoenergetic images.

In all of the 79 patients (38% osteoporosis) , the AUC of monoenergetic-image-based BMD was 0.858 (95% CI: 0.773-0.943). At maximum value of Youden's index ($J = 0.616$), sensitivity and specificity were found to be 0.800 and 0.816, respectively. In both, monoenergetic-image- and QCT-based measurements, patients with vertebral fractures had significantly lower BMD than patients without osteoporotic fractures (monoenergetic-image-based: median difference, 56.39 mg/cm^3, $p < 0.001$ and QCT-based: 58.16 mg/cm^3, $p < 0.001$).

4.3. Material decomposition

X-ray attenuation represented in the CT image can be regarded as a summation of materials with the product of their volume fractions and mass attenuation coefficient:

$$\frac{\mu(E)}{\rho} = \Sigma_i f_i \frac{\mu_i(E)}{\rho_i}, \tag{4.20}$$

where f_i is the volume fraction of the material i, whose mass attenuation coefficient is represented as $\mu_i(E)/\rho_i$ at the X-ray energy E. Mass attenuation coefficient can generally be obtained from NIST-database. $\mu(E)/\rho$ is the linear coefficient represented in the CT image, which has the following conversion with HU:

$$\frac{\mu(E)}{\rho} = \frac{\mu_w(E)}{\rho_w}(\frac{\mathrm{HU}(E)}{1000} + 1), \tag{4.21}$$

where $\mu_w(E)/\rho_w$ is a constant representing the mass attenuation coefficient of water at the X-ray energy E, $\mathrm{HU}(E)$ is the HU in the monoenergetic image E.

In a dual-energy based multi-energy CT system, provided there are two image signals obtained, the solution of solving volume fractions, f_A and f_B, is mathematically defined, provided these two materials are known.

$$\frac{\mu(E_H)}{\rho} = f_1 \frac{\mu_1(E_H)}{\rho_1} + f_2 \frac{\mu_2(E_H)}{\rho_2}, \tag{4.22}$$

$$\frac{\mu(E_L)}{\rho} = f_1 \frac{\mu_1(E_L)}{\rho_1} + f_2 \frac{\mu_2(E_L)}{\rho_2}, \tag{4.23}$$

where E_H and E_L represent two energies at low and high keV.

This two-material decomposition application was investigated and the result was published in **journal publication J-15**, where the fraction of gadolinium solution is decomposed from water in laboratory-made phantoms and from blood fraction in an animal experiment. In this study, gadolinium contrast agent (Dotarem, Guerbet AG, Zürich, Switzerland) solution was prepared in concentration of 20, 15, 10, 5, 2, 1 mg/ml (in laboratory-prepared centrifuge tubes) and scanned in dual-layered based CT. Repetitive scans were made with 120 kVp at high X-ray radiation dose (1000 mAs) and low dose (100 mAs). Compared against known concentrations, a high correlation coefficient ($r > 0.999$) was found with decomposed concentration. No significant difference was found between repeated scans ($p > 0.05$). The accuracy of decomposed gadolinium stayed below 0.17 mg/ml for all measurements.

Experiments performed in a pig with gadolinium injection also proved the feasibility of the decomposition in in-vivo CT scans.

In addition, three-material decomposition was studied with the assumption of volume conservation, where all volume fractions sum up to 1:

$$\frac{\mu(E_H)}{\rho} = f_1 \frac{\mu_1(E_H)}{\rho_1} + f_2 \frac{\mu_2(E_H)}{\rho_2} + f_3 \frac{\mu_3(E_H)}{\rho_3}, \tag{4.24}$$

$$\frac{\mu(E_L)}{\rho} = f_1 \frac{\mu_1(E_L)}{\rho_1} + f_2 \frac{\mu_2(E_L)}{\rho_2} + f_3 \frac{\mu_3(E_L)}{\rho_3}, \tag{4.25}$$

with the condition that

$$f_1 + f_2 + f_3 = 1. \tag{4.26}$$

This three-material decomposition was evaluated and published in **journal publication J-10**, where the fractions of calcium (HA), lipid (representing yellow bone marrow) and water (representing red bone marrow) were decomposed in CT scans of in-vivo human spine (in total of 27 patients with and without conditions affecting bone or fat metabolism). Because of the complexity of the actual bone components, only the dominating fractions (yellow or red bone marrow, i.e. fat or water fractions) inside patients' vertebrae were determined, instead of investigating the numerical accuracy. The dominating bone marrows were compared to MRI images of the corresponding patients, as a standard of reference, Figure 4.11. The sensitivity (0.93–0.95) and specificity (0.89) of three-material decomposed images were substantially higher than conventional CT (0.73–0.76 and 0.78–0.83, respectively), in the context of diagnosing bone edema and fresh/acute vertebral fractures.

4.4. Discussion

This chapter evaluates multi-energy CT in musculoskeletal imaging, specifically dual-layer CT, which provides novel assessments of bone status compared to conventional CT. These clinical applications can also be applied to other dual-energy techniques such as dual-source, split beam and kVP switch systems.

Material quantification and decomposition described in this chapter are sensitive to radiation dose, patient size and image noise. As the result in Section 4.2.1 reports, a dose below 50 mAs leads to less reliable results. This can be a very

(a) Conventional CT **(b)** Conventional MRI

(c) Water fraction **(d)** Fat fraction

Figure 4.11.: Material decomposition in dual-energy CT

Top left: conventional CT with two fracture site (T8, T9). Top right: MRI of the fractures showing T8 is an aged fracture and T9 is a fresh fracture with edema. Bottom left: water fraction decomposed from DECT. Bottom right: fat fraction decomposed from DECT. The fresh fracture has an increased water fraction. These fraction images provide information of the fracture age similar to MRI. These images were published in J-10.

challenging point for further studies in ultra-low-dose CT. Novel techniques, such as sparse sampling discussed in previous chapters, may be helpful.

BMD estimation in dual-energy CT as an opportunistic osteoporosis-screening method is limited to the application of contrast agents. Certain scanning protocols are operated with oral or intravenous contrast agent. Contrast agents have the same range or higher density compared to human bone thus making the quantification inaccurate.

Material decomposition is very attractive in clinical research however, it has the main weakness that the composition of materials must be known. Because human bone is a very complicated organ and differs individually, a correct in-vivo decomposition may be unlikely possible, especially for three material decomposition. Moreover, like quantification, decomposition in multi-energy CT is very susceptible to image noise and very difficult in low dose conditions.

Part II.

Summary of Publications

J-I: Is multidetector CT-based bone mineral density and quantitative bone microstructure assessment at the spine still feasible using ultra-low tube current and sparse sampling?

The publication entitled *Is multidetector CT-based bone mineral density and quantitative bone microstructure assessment at the spine still feasible using ultra-low tube current and sparse sampling?* was published in European Radiology (ISSN: 0938-7994). The manuscript was authored by Kai Mei, Felix K. Kopp, Rolf Bippus, Thomas Köhler, Benedikt J. Schwaiger, Alexandra S. Gersing, Alexander Fehringer, Andreas Sauter, Daniela Pfeiffer, Franz Pfeiffer, Ernst J. Rummeny, Jan S. Kirschke, Peter B. Noël and Thomas Baum.

Abstract

Purpose

Osteoporosis diagnosis using multidetector CT (MDCT) is limited to relatively high radiation exposure. We investigated the effect of simulated ultra-low-dose protocols on in-vivo bone mineral density (BMD) and quantitative trabecular bone assessment.

Methods

Institutional review board approval was obtained. Twelve subjects with osteoporotic vertebral fractures and 12 age- and gender-matched controls undergoing routine

thoracic and abdominal MDCT were included (average effective dose: 10 mSv). Ultra-low radiation examinations were achieved by simulating lower tube currents and sparse samplings at 50%, 25% and 10% of the original dose. BMD and trabecular bone parameters were extracted in T10-L5.

Results

Except for BMD measurements in sparse sampling data, absolute values of all parameters derived from ultra-low-dose data were significantly different from those derived from original dose images ($p < 0.05$). BMD, apparent bone fraction and trabecular thickness were still consistently lower in subjects with than in those without fractures ($p < 0.05$).

Conclusion

In ultra-low-dose scans, BMD and microstructure parameters were able to differentiate subjects with and without vertebral fractures, suggesting osteoporosis diagnosis is feasible. However, absolute values differed from original values. BMD from sparse sampling appeared to be more robust. This dose-dependency of parameters should be considered for future clinical use.

J-II: Bone mineral density measurements in vertebral specimens and phantoms using dual-layer spectral computed tomography

The publication entitled *BMD measurements in vertebral specimens and phantoms using dual-layer spectral computed tomography* was published in Scientific reports (ISSN: 2045-2322). The manuscript was authored by Kai Mei, Benedikt J. Schwaiger, Felix K. Kopp, Sebastian Ehn, Alexandra S. Gersing, Jan S. Kirschke, Daniela. Muenzel, Alexander A. Fingerle, Ernst J. Rummeny, Franz Pfeiffer, Thomas Baum, Peter B. Noel.

Abstract

Purpose

To assess whether phantomless calcium-hydroxyapatite (HA) specific bone mineral density (BMD) measurements with dual-layer spectral computed tomography are accurate in phantoms and vertebral specimens.

Methods

Ex-vivo human vertebrae ($n = 13$) and a phantom containing different known HA concentrations were placed in a semi-anthropomorphic abdomen phantom with different extension rings simulating different degrees of obesity. Phantomless dual-layer spectral CT was performed at different tube current settings (500, 250, 125 and 50 mAs). HA-specific BMD was derived from spectral-based virtual monoenergetic images at 50 keV and 200 keV. Values were compared to the HA

concentrations of the phantoms and conventional qCT measurements using a reference phantom, respectively.

Results

Above 125 mAs, errors for phantom measurements ranged between -1.3% to 4.8%, based on spectral information. In vertebral specimens, high correlations were found between BMD values assessed with spectral CT and conventional qCT (r ranging between 0.96 and 0.99; $p < 0.001$ for all) with different extension rings, and a high agreement was found in Bland Altman plots. Different degrees of obesity did not have a significant influence on measurements ($p > 0.05$ for all).

Conclusion

These results suggest a high validity of HA-specific BMD measurements based on dual-layer spectral CT examinations in setups simulating different degrees of obesity without the need for a reference phantom, thus demonstrating their feasibility in clinical routine.

J-III: Dual-layer spectral computed tomography: measuring relative electron density

The publication entitled *Dual-layer spectral computed tomography: measuring relative electron density* was published in European Radiology Experimental (ISSN: 2509-9280). The manuscript was authored by Kai Mei, Sebastian Ehn, Markus Oechsner, Felix K. Kopp, Daniela Pfeiffer, Alexander A. Fingerle, Franz Pfeiffer, Stepahnie E. Combs, Jan J. Wilkens, Ernst J. Rummeny, Peter B. Noël.

Abstract

Purpose

X-ray and particle radiation therapy planning requires accurate estimation of local electron density within the patient body to calculate dose delivery to tumour regions. We evaluate the feasibility and accuracy of electron density measurement using dual-layer computed tomography (DLCT), a recently introduced dual-energy CT technique.

Methods

Two calibration phantoms were scanned with DLCT and virtual monoenergetic images (VMIs) at 50 keV and 200 keV were generated. We investigated two approaches to obtain relative electron densities from these VMIs: to fit an analytic interaction cross-sectional model and to empirically calibrate a conversion function

with one of the phantoms. Knowledge of the emitted x-ray spectrum was not required for the presented work.

Results

The results from both methods were highly correlated to the nominal values ($R > 0.999$). Except for the water and lung inserts, the error was within 1.79% (average 1.53%) for the cross-sectional model and 1.61% (average 0.87%) for the calibrated conversion. Different radiation doses did not have a significant influence on the measurement ($p = 0.348, 0.167$), suggesting that the methods are reproducible. Further, we applied these methods to routine clinical data.

Conclusions

Our study shows a high validity of electron density estimation based on DLCT, which has potential to improve the procedure and accuracy of measuring electron density in clinical practice.

Publications as co-author

J-1: Effect of low-dose and iterative reconstruction on trabecular bone microstructure assessment

We investigated the effects of low-dose multi detector computed tomography (MDCT) in combination with statistical iterative reconstruction algorithms on trabecular bone microstructure parameters.

Twelve donated vertebrae were scanned with the routine radiation exposure used in our department (standard-dose) and a low-dose protocol. Reconstructions were performed with filtered backprojection (FBP) and maximum-likelihood based statistical iterative reconstruction (SIR). Trabecular bone microstructure parameters were assessed and statistically compared for each reconstruction. Moreover, fracture loads of the vertebrae were biomechanically determined and correlated to the assessed microstructure parameters.

Trabecular bone microstructure parameters based on low-dose MDCT and SIR significantly correlated with vertebral bone strength. There was no significant difference between microstructure parameters calculated on low-dose SIR and standard-dose FBP images. However, the results revealed a strong dependency on the regularization strength applied during SIR. It was observed that stronger regularization might corrupt the microstructure analysis, because the trabecular structure is a very small detail that might get lost during the regularization process.

As a consequence, the introduction of SIR for trabecular bone microstructure analysis requires a specific optimization of the regularization parameters. Moreover, in comparison to other approaches, superior noise-resolution trade-offs can be found with the proposed methods.

J-2: Effects of dose reduction on bone strength prediction using finite element analysis

This study aimed to evaluate the effect of dose reduction, by means of tube exposure reduction, on bone strength prediction from finite-element (FE) analysis.

Fresh thoracic mid-vertebrae specimens ($n = 11$) were imaged, using multi-detector computed tomography (MDCT), at different intensities of X-ray tube exposures (80, 150, 220 and 500 mAs). Bone mineral density (BMD) was estimated from the mid-slice of each specimen from MDCT images. Differences in image quality and geometry of each specimen were measured. FE analysis was performed on all specimens to predict fracture load. Paired t-tests were used to compare the results obtained, using the highest CT dose (500 mAs) as reference.

Dose reduction had no significant impact on FE-predicted fracture loads, with significant correlations obtained with reference to 500 mAs, for 80 mAs ($R^2 = 0.997$, $p < 0.001$), 150 mAs ($R^2 = 0.998, p < 0.001$) and 220 mAs ($R^2 = 0.987, p < 0.001$). There were no significant differences in volume quantification between the different doses examined. CT imaging radiation dose could be reduced substantially to 64% with no impact on strength estimates obtained from FE analysis.

Reduced CT dose will enable early diagnosis and advanced monitoring of osteoporosis and associated fracture risk.

J-3: A post-processing algorithm for spectral CT material selective images using learned dictionaries

In spectral computed tomography (spectral CT), the additional information about the energy dependence of the linear attenuation coefficients can be exploited to produce material selective images. These images have proven to be useful for various applications such as quantitative imaging or clinical diagnosis. However, noise amplification on material decomposed images remains a fundamental problem which limits the utility of basis material images.

In this work, we present a new post-processing algorithm for material selective images which is based on dictionary denoising and specifically tailored to take the properties of the basis material images into account. Dictionary denoising is a powerful noise reduction technique which separates image features from noise by modeling small image patches as a sparse linear combination of dictionary atoms. These dictionary atoms are learned from training images prior to the denoising process. We have adapted the dictionary denoising algorithm to make use of the structural correlation as well as the anti-correlated noise which is typically present in material selective images.

Dictionary denoising is first applied to the virtual monochromatic image for which the anti-correlated noise maximally cancels out (minimum noise image) in order to identify the structures and edges of the material selective images. In a second step, the basis material images are compiled by finding local linear transformations between the minimum noise image and the basis material images. Numerical simulations as well as an experimental measurement show that our algorithm achieves improved image quality compared to two other post-processing methods, namely conventional dictionary denoising and bilateral filtering. As a post-processing method, it can be combined with image-based as well as projection-based material decomposition techniques.

Our algorithm therefore has the potential to improve the usability of basis material images for various tasks such as artifact reduction, quantitative imaging and clinical diagnosis.

J-4: Assessment of quantification accuracy and image quality of a full-body dual-layer spectral CT system

The performance of a recently introduced spectral computed tomography system based on a dual-layer detector has been investigated.

A semi-anthropomorphic abdomen phantom for CT performance evaluation was imaged on the dual-layer spectral CT at different radiation exposure levels (CTDIvol of 10 mGy, 20 mGy and 30 mGy). The phantom was equipped with specific low-contrast and tissue-equivalent inserts including water-, adipose-, muscle-, liver-, bone-like materials and a variation in iodine concentrations. Additionally, the phantom size was varied using different extension rings to simulate different patient sizes. Contrast-to-noise (CNR) ratio over the range of available virtual mono-energetic images (VMI) and the quantitative accuracy of VMI Hounsfield Units (HU), effective-Z maps and iodine concentrations have been evaluated. Central and peripheral locations in the field-of-view have been examined.

For all evaluated imaging tasks the results are within the calculated theoretical range of the tissue-equivalent inserts. Especially at low energies, the CNR in VMIs could be boosted by up to 330% with respect to conventional images using iDose/spectral reconstructions at level 0. The mean bias found in effective-Z maps and iodine concentrations averaged over all exposure levels and phantom sizes was 1.9% (eff. Z) and 3.4% (iodine). Only small variations were observed with increasing phantom size (+3%) while the bias was nearly independent of the exposure level (±0.2%).

Therefore, dual-layer detector based CT offers high quantitative accuracy of spectral images over the complete field-of-view without any compromise in radiation dose or diagnostic image quality.

J-5: Feasibility of opportunistic osteoporosis screening in routine contrast-enhanced multi detector computed tomography (MDCT) using texture analysis

This study investigated the feasibility of opportunistic osteoporosis screening in routine contrast-enhanced MDCT exams using texture analysis. The results showed an acceptable reproducibility of texture features, and these features could discriminate healthy/osteoporotic fracture cohort with an accuracy of 83%.

This aim of this study is to investigate the feasibility of opportunistic osteoporosis screening in routine contrast-enhanced MDCT exams using texture analysis.

We performed texture analysis at the spine in routine MDCT exams and investigated the effect of intravenous contrast medium (IVCM) ($n = 7$), slice thickness ($n = 7$), the long-term reproducibility ($n = 9$), and the ability to differentiate healthy/osteoporotic fracture cohort ($n = 9$ age and gender matched pairs). Eight texture features were extracted using gray level co-occurrence matrix (GLCM). The independent sample t test was used to rank the features of healthy/fracture cohort and classification was performed using support vector machine (SVM).

The results revealed significant correlations between texture parameters derived from MDCT scans with and without IVCM (r up to 0.91) slice thickness of 1 mm versus 2 and 3 mm (r up to 0.96) and scan-rescan (r up to 0.59). The performance of the SVM classifier was evaluated using 10-fold cross-validation and revealed an average classification accuracy of 83%.

Opportunistic osteoporosis screening at the spine using specific texture parameters (energy, entropy, and homogeneity) and SVM can be performed in routine contrast-enhanced MDCT exams.

J-6: Effect of radiation dose reduction on texture measures of trabecular bone microstructure: an in-vitro study

Osteoporosis is characterized by bone loss and degradation of bone microstructure leading to fracture particularly in elderly people. Osteoporotic bone degeneration and fracture risk can be assessed by bone mineral density and trabecular bone score from 2D projection dual-energy X-ray absorptiometry images. However, multidetector computed tomography image based quantification of trabecular bone microstructure showed significant improvement in prediction of fracture risk beyond that from bone mineral density and trabecular bone score; however, high radiation exposure limits its use in routine clinical in vivo examinations. Hence, this study investigated reduction of radiation dose and its effects on image quality of thoracic midvertebral specimens.

Twenty-four texture features were extracted to quantify the image quality from multidetector computed tomography images of 11 thoracic midvertebral specimens, by means of statistical moments, the gray-level co-occurrence matrix, and the gray-level run-length matrix, and were analyzed by an independent sample t-test to observe differences in image texture with respect to radiation doses of 80, 150, 220, and 500 mAs.

The results showed that three features-namely, global variance, energy, and run percentage, were not statistically significant ($p > 0.05$) for low doses with respect to 500 mAs.

Hence, it is evident that these three dose-independent features can be used for disease monitoring with a low-dose imaging protocol.

J-7: Multidetector computed tomography imaging: effect of sparse sampling and iterative reconstruction on trabecular bone microstructure

Multidetector computed tomography-based trabecular bone microstructure analysis ensures promising results in fracture risk prediction caused by osteoporosis. Because multidetector computed tomography is associated with high radiation exposure, its clinical routine use is limited.

Hence, in this study, we investigated in 11 thoracic midvertebral specimens whether trabecular texture parameters are comparable derived from (1) images reconstructed using statistical iterative reconstruction (SIR) and filtered back projection as criterion standard at different exposures (80, 150, 220, and 500 mAs) and (2) from SIR-based sparse sampling projections (12.5%, 25%, 50%, and 100%) and equivalent exposures as criterion standard. Twenty-four texture features were computed, and those that showed similar values between (1) filtered back projection and SIR at the different exposure levels and (2) sparse sampling and equivalent exposures and reconstructed with SIR were identified. These parameters can be of equal value in determining trabecular bone microstructure with lower radiation exposure using sparse sampling and SIR.

J-8: MDCT-based finite element analysis of vertebral fracture risk: what dose is needed?

The aim of this study was to compare vertebral failure loads, predicted from finite element (FE) analysis of patients with and without osteoporotic vertebral fractures (OVF) at virtually reduced dose levels, compared to standard-dose exposure from multidetector computed tomography (MDCT) imaging and evaluate whether ultra-low dose derived FE analysis can still differentiate patient groups.

An institutional review board (IRB) approval was obtained for this retrospective study. A total of 16 patients were evaluated at standard-dose MDCT; eight with and eight without OVF. Images were reconstructed at virtually reduced dose levels (i.e. half, quarter and tenth of the standard dose). Failure load was determined at L1-3 from FE analysis and compared between standard, half, quarter, and tenth doses and used to differentiate between fracture and control groups.

Failure load derived at standard dose (3254 ± 909 N and 3794 ± 984 N) did not significantly differ from half (3390 ± 890 N and 3860 ± 1063 N) and quarter dose (3375 ± 915 N and 3925 ± 990 N) but was significantly higher for one tenth dose (4513 ± 1762 N and 4766 ± 1628 N) for fracture and control groups, respectively. Failure load differed significantly between the two groups at standard, half and quarter doses, but not at tenth dose. Receiver operating characteristic (ROC) curve analysis also demonstrated that standard, half, and quarter doses can significantly differentiate the fracture from the control group.

The use of MDCT enables a dose reduction of at least 75% compared to standard-dose for an adequate prediction of vertebral failure load based on non-invasive FE analysis.

J-9: Effect of statistically iterative image reconstruction on vertebral bone strength prediction using bone mineral density and finite element modeling - a preliminary study

Statistical iterative reconstruction (SIR) using multidetector computed tomography (MDCT) is a promising alternative to standard filtered back projection (FBP), because of lower noise generation while maintaining image quality. Hence, we investigated the feasibility of SIR in predicting MDCT-based bone mineral density (BMD) and vertebral bone strength from finite element (FE) analysis.

The BMD and FE-predicted bone strength derived from MDCT images reconstructed using standard FBP (FFBP) and SIR with (FSIR) and without regularization (FSIRB0) were validated against experimental failure loads (Fexp).

Statistical iterative reconstruction produced the best quality images with regard to noise, signal-to-noise ratio, and contrast-to-noise ratio. Fexp significantly correlated with FFBP, FSIR, and FSIRB0. FFBP had a significant correlation with FSIRB0 and FSIR. The BMD derived from FBP, SIRB0, and SIR were significantly correlated. Effects of regularization should be further investigated with FE and BMD analysis to allow for an optimal iterative reconstruction algorithm to be implemented in an in-vivo scenario.

J-10: Three-material decomposition with dual-layer spectral CT compared to MRI for the detection of bone marrow edema in patients with acute vertebral fractures

To assess whether bone marrow edema in patients with acute vertebral fractures can be accurately diagnosed based on three-material decomposition with dual-layer spectral CT (DLCT).

Acute ($n = 41$) and chronic ($n = 18$) osteoporotic thoracolumbar vertebral fractures as diagnosed by MRI (hyperintense signal in STIR sequences) in 27 subjects (72 ± 11 years; 17 women) were assessed with DLCT. Spectral data were decomposed into hydroxyapatite, edema-equivalent, and fat-equivalent density maps using an in-house-developed algorithm. Two radiologists, blinded to clinical and MR findings, assessed DLCT and conventional CT independently, using a Likert scale (1 = no edema; 2 = likely no edema; 3 = likely edema; 4 = edema). For DLCT and conventional CT, accuracy, sensitivity, and specificity for identifying acute fractures (Likert scale, 3 and 4) were analyzed separately using MRI as standard of reference.

For the identification of acute fractures, conventional CT showed a sensitivity of 0.73-0.76 and specificity of 0.78-0.83, whereas the sensitivity (0.93-0.95) and specificity (0.89) of decomposed DLCT images were substantially higher. Accuracy increased from 0.76 for conventional CT to 0.92-0.93 using DLCT. Interreader agreement for fracture assessment was high in conventional CT (weighted κ [95% confidence interval]; 0.81 [0.70; 0.92]) and DLCT (0.96 [0.92; 1.00]).

Material decomposition of DLCT data substantially improved accuracy for the diagnosis of acute vertebral fractures, with a high interreader agreement. This may spare patients additional examinations and facilitate the diagnosis of vertebral fractures.

J-11: Effects of virtual tube current reduction and sparse sampling on MDCT-based femoral BMD measurements

This study investigates the impact of tube current reduction and sparse sampling on femoral bone mineral density (BMD) measurements derived from multi-detector computed tomography (MDCT). The application of sparse sampling led to robust and clinically acceptable BMD measurements. In contrast, BMD measurements derived from MDCT with virtually reduced tube currents showed a considerable increase when compared to original data.

The study aims to evaluate the effects of radiation dose reduction by using virtual reduction of tube current or sparse sampling combined with standard filtered back projection (FBP) and statistical iterative reconstruction (SIR) on femoral bone mineral density (BMD) measurements derived from multi-detector computed tomography (MDCT).

In routine MDCT scans of 41 subjects (65.9% men; age 69.3 ± 10.1 years), reduced radiation doses were simulated by lowering tube currents and applying sparse sampling (50, 25, and 10% of the original tube current and projections, respectively). Images were reconstructed using FBP and SIR. BMD values were assessed in the femoral neck and compared between the different dose levels, numbers of projections, and image reconstruction approaches.

Compared to full-dose MDCT, virtual lowering of the tube current by applying our simulation algorithm resulted in increases in BMD values for both FBP (up to a relative change of 32.5%) and SIR (up to a relative change of 32.3%). In contrast, the application of sparse sampling with a reduction down to 10% of projections showed robust BMD values, with clinically acceptable relative changes of up to 0.5% (FBP) and 0.7% (SIR).

Our simulations, which still require clinical validation, indicate that reductions down to ultra-low tube currents have a significant impact on MDCT-based femoral BMD measurements. In contrast, the application of sparse-sampled MDCT seems a promising future clinical option that may enable a significant reduction of the radiation dose without considerable changes of BMD values.

J-12: Multi-detector CT imaging: impact of virtual tube current reduction and sparse sampling on detection of vertebral fractures

To systematically evaluate the effects of virtual tube current reduction and sparse sampling on image quality and vertebral fracture diagnostics in multi-detector computed tomography (MDCT).

In routine MDCT scans of 35 patients (80.0% females, 70.6 ± 14.2 years, 65.7% showing vertebral fractures), reduced radiation doses were retrospectively simulated by virtually lowering tube currents and applying sparse sampling, considering 50%, 25%, and 10% of the original tube current and projections, respectively. Two readers evaluated items of image quality and presence of vertebral fractures. Readout between the evaluations in the original images and those with virtually lowered tube currents or sparse sampling were compared.

A significant difference was revealed between the evaluations of image quality between MDCT with virtually lowered tube current and sparse-sampled MDCT ($p < 0.001$). Sparse-sampled data with only 25% of original projections still showed good to very good overall image quality and contrast of vertebrae as well as minimal artifacts. There were no missed fractures in sparse-sampled MDCT with 50% reduction of projections, and clinically acceptable determination of fracture age was possible in MDCT with 75% reduction of projections, in contrast to MDCT with 50% or 75% virtual tube current reduction, respectively.

Sparse-sampled MDCT provides adequate image quality and diagnostic accuracy for vertebral fracture detection with 50% of original projections in contrast to corresponding MDCT with lowered tube current. Thus, sparse sampling is a promising technique for dose reductions in MDCT that could be introduced in future generations of scanners.

J-13: Tube current reduction in computed tomography angiography - how low can we go in patients with suspected acute stroke?

To systematically evaluate image quality, detectability of large vessel occlusion (LVO) or dissection, and diagnostic confidence in computed tomography angiography (CTA) with virtually lowered tube current and iterative reconstruction (IR) in patients with suspected acute stroke.

Thirty patients (50% with LVO or dissection) underwent CTA of the supraaortal up to the intracranial arterial vessels. CTA scans were simulated as if they were made at 50% (D50), 25% (D25), and 10% (D10) of the original tube current. Image reconstruction was achieved with two levels of IR (A: similar to clinical reconstructions, B: two times stronger regularization). Two readers performed qualitative image evaluation considering overall image quality, artifacts, vessel contrast, detection of vessel pathology, and diagnostic confidence.

Level B of IR was favorable regarding overall image quality and artifacts for D10, while level A was favorable for D100 and D50. CTA scans with D25 and both levels of IR still showed good vessel contrast, with even peripheral arterial branches of the anterior, middle, and posterior cerebral artery being clearly detectable. Further, CTA scans with D25 using level A of IR showed an adequate level of diagnostic confidence without any missed LVO or dissection according to evaluations of both readers.

CTA using IR and tube currents lowered down to 25% of original imaging is feasible without drawbacks regarding vessel contrast or detection of vessel pathology in patients with suspected acute stroke. Thus, our approach enables significant reductions in radiation exposure for patients undergoing head and neck CTA.

J-14: Bone mineral density measurements derived from dual-layer spectral CT enable opportunistic screening for osteoporosis

To investigate the in vivo applicability of non-contrast-enhanced hydroxyapatite (HA)-specific bone mineral density (BMD) measurements based on dual-layer CT (DLCT).

A spine phantom containing three artificial vertebral bodies with known HA densities was measured to obtain spectral data using DLCT and quantitative CT (QCT), simulating different patient positions and grades of obesity. BMD was calculated from virtual monoenergetic images at 50 and 200 keV. HA-specific BMD values of 174 vertebrae in 33 patients (66 ± 18 years; 33% women) were determined in non-contrast routine DLCT and compared with corresponding QCT-based BMD values.

Examining the phantom, HA-specific BMD measurements were on a par with QCT measurements. In vivo measurements revealed strong correlations between DLCT and QCT ($r = 0.987$ [95% confidence interval, 0.963 - 1.000]; $p < 0.001$) and substantial agreement in a Bland–Altman plot.

DLCT-based HA-specific BMD measurements were comparable with QCT measurements in in vivo analyses. This suggests that opportunistic DLCT-based BMD measurements are an alternative to QCT, without requiring phantoms and specific protocols.

J-15: Perfusion-ventilation CT via three-material differentiation in dual-layer CT: a feasibility study

Dual-Energy Computed Tomography is of significant clinical interest due to the possibility of material differentiation and quantification. In current clinical routine, primarily two materials are differentiated, e.g., iodine and soft-tissue. A ventilation-perfusion-examination acquired within a single CT scan requires two contrast agents, e.g., xenon and gadolinium, and a three-material differentiation. In the current study, we have developed a solution for three-material differentiation for a ventilation-perfusion-examination.

A landrace pig was examined using a dual-layer CT, and three scans were performed: 1) native; 2) xenon ventilation only; 3) xenon ventilation and gadolinium perfusion. An in-house developed algorithm was used to obtain xenon- and gadolinium-density maps. Firstly, lung tissue was segmented from other tissue. Consequently, a two-material decomposition was performed for lung tissue (xenon/soft-tissue) and for remaining tissue (gadolinium/soft-tissue).

Results reveal that it was possible to differentiate xenon and gadolinium in a ventilation/perfusion scan of a pig, resulting in xenon and gadolinium density maps. By summation of both density maps, a three-material differentiation (xenon/gadolinium/soft tissue) can be performed and thus, xenon ventilation and gadolinium perfusion can be visualized in a single CT scan. In an additionally performed phantom study, xenon and gadolinium quantification showed very accurate results ($r > 0.999$ between measured and known concentrations).

C-1: Effect of low-dose and iterative reconstruction on trabecular bone microstructure assessment

The trabecular bone microstructure is an important factor in the development of osteoporosis. It is well known that its deterioration is one effect when osteoporosis occurs. Previous research showed that the analysis of trabecular bone microstructure enables more precise diagnoses of osteoporosis compared to a sole measurement of the mineral density. Microstructure parameters are assessed on volumetric images of the bone acquired either with high-resolution magnetic resonance imaging, high-resolution peripheral quantitative computed tomography or high-resolution computed tomography (CT), with only CT being applicable to the spine, which is one of clinically most relevant fracture sites. However, due to the high radiation exposure for imaging the whole spine these measurements are not applicable in current clinical routine.

In this work, twelve vertebrae from three different donors were scanned with standard and low radiation dose. Trabecular bone microstructure parameters were assessed for CT images reconstructed with statistical iterative reconstruction (SIR) and analytical filtered backprojection (FBP).

The resulting structure parameters were correlated to the biomechanically determined fracture load of each vertebra. Microstructure parameters assessed for low-dose data reconstructed with SIR significantly correlated with fracture loads as well as parameters assessed for standard-dose data reconstructed with FBP. Ideal results were achieved with low to zero regularization strength yielding microstructure parameters not significantly different from those assessed for standard-dose FPB data. Moreover, in comparison to other approaches, superior noise-resolution trade-offs can be found with the proposed methods.

C-2: Dictionary-based image denoising for dual energy computer tomography

Compared to conventional computed tomography (CT), dual energy CT allows for improved material decomposition by conducting measurements at two distinct energy spectra. Since radiation exposure is a major concern in clinical CT, there is a need for tools to reduce the noise level in images while preserving diagnostic information. One way to achieve this goal is the application of image-based denoising algorithms after an analytical reconstruction has been performed.

We have developed a modified dictionary denoising algorithm for dual energy CT aimed at exploiting the high spatial correlation between between images obtained from different energy spectra. Both the low-and high energy image are partitioned into small patches which are subsequently normalized. Combined patches with improved signal-to-noise ratio are formed by a weighted addition of corresponding normalized patches from both images. Assuming that corresponding low-and high energy image patches are related by a linear transformation, the signal in both patches is added coherently while noise is neglected. Conventional dictionary denoising is then performed on the combined patches.

Compared to conventional dictionary denoising and bilateral filtering, our algorithm achieved superior performance in terms of qualitative and quantitative image quality measures.

We demonstrate, in simulation studies, that this approach can produce 2d-histograms of the high- and low-energy reconstruction which are characterized by significantly improved material features and separation. Moreover, in comparison to other approaches that attempt denoising without simultaneously using both energy signals, superior similarity to the ground truth can be found with our proposed algorithm.

C-3: Effects of sparse sampling in combination with iterative reconstruction on quantitative bone microstructure assessment

The trabecular bone microstructure is a key to the early diagnosis and advanced therapy monitoring of osteoporosis. Regularly measuring bone microstructure with conventional multi-detector computer tomography (MDCT) would expose patients with a relatively high radiation dose.

One possible solution to reduce exposure to patients is sampling fewer projection angles. This approach can be supported by advanced reconstruction algorithms, with their ability to achieve better image quality under reduced projection angles or high levels of noise.

In this work, we investigated the performance of iterative reconstruction from sparse sampled projection data on trabecular bone microstructure in in-vivo MDCT scans of human spines. The computed MDCT images were evaluated by calculating bone microstructure parameters.

We demonstrated that bone microstructure parameters were still computationally distinguishable when half or less of the radiation dose was employed.

C-4: Calcium decomposition and phantomless bone mineral density measurements using dual-layer-based spectral computed tomography

Dual-layer spectral computed tomography (CT) provides a novel clinically available concept for material decomposition (calcium hydroxyapatite, HA) and thus to estimate the bone mineral density (BMD) based on non-dedicated clinical examinations. In this study, we assessed whether HA specific BMD measurements with dual-layer spectral CT are accurate in phantoms and vertebral specimens.

Dual-layer spectral CT was performed at different tube current settings (500, 250, 125 and 50 mAs) with a tube voltage of 120 kVp. Ex-vivo human vertebrae ($n = 13$) and a phantom containing different known HA concentrations were placed in a semi-anthropomorphic abdomen phantom. BMD was derived with an in-house developed algorithm from spectral-based virtual monoenergetic images at 50 keV and 200 keV. Values were compared to the HA concentrations of the phantoms and conventional quantitative CT (QCT) measurements using a reference phantom, respectively.

Above 125 mAs, which is the radiation exposure level of clinical examinations, errors for phantom measurements based on spectral information were less than 5%, compared to known concentrations. In vertebral specimens, high correlations were found between BMD values assessed with spectral CT and conventional QCT (correlation coefficients > 0.96; $p < 0.001$ for all).

These results suggest a high accuracy of quantitate HA-specific BMD measurements based on dual-layer spectral CT examinations without the need for a reference phantom, thus demonstrating their feasibility in clinical routine.

C-5: Advancements in computed tomography for musculoskeletal imaging

Recent advancements in the field of computed tomography (CT) showed promising results for the application in musculoskeletal (MSK) imaging. Iterative reconstruction techniques and the resulting capability of dose reduction proofed to be eligible for osteoporosis diagnosis and (therapy) monitoring in clinical routine. Spectral CT allows for phantomless assessment of BMD and advanced tissue decomposition, predicting fracture risk in non-dedicated routine examinations or recognizing acute from old vertebral fractures. The potential introduction of new sparse sampling acquisition schemes could even enhance the quality of the mentioned techniques for low dose MSK imaging. In this work, we present an overview of our recent CT developments for MSK imaging and provide an outlook over promising future technologies.

List of Figures

List of Tables

Bibliography

[1] D. Bliuc, N. D. Nguyen, V. E. Milch, T. V. Nguyen, and J. A. Eisman. “Mortality risk associated with low-trauma osteoporotic fracture and subsequent fracture in men and women.” In: *Jama* 301.5 (2009), pp. 513–521.

[2] G. Ioannidis, A. Papaioannou, W. M. Hopman, N. Akhtar-Danesh, T. Anastassiades, L. Pickard, C. C. Kennedy, J. C. Prior, W. P. Olszynski, K. S. Davison, et al. “Relation between fractures and mortality: results from the Canadian Multicentre Osteoporosis Study.” In: *Cmaj* 181.5 (2009), pp. 265–271.

[3] B. Häussler, H. Gothe, D. Göl, G. Glaeske, L. Pientka, and D. Felsenberg. “Epidemiology, treatment and costs of osteoporosis in Germany—the BoneEVA Study.” In: *Osteoporosis International* 18.1 (2007), pp. 77–84.

[4] I. Hallberg, M. Bachrach-Lindström, S. Hammerby, G. Toss, and A.-C. Ek. “Health-related quality of life after vertebral or hip fracture: a seven-year follow-up study.” In: *BMC musculoskeletal disorders* 10.1 (2009), p. 135.

[5] S. Schuit, M. Van der Klift, A. Weel, C. De Laet, H. Burger, E. Seeman, A. Hofman, A. Uitterlinden, J. Van Leeuwen, and H. Pols. “Fracture incidence and association with bone mineral density in elderly men and women: the Rotterdam Study.” In: *Bone* 34.1 (2004), pp. 195–202.

[6] E. S. Siris, Y.-T. Chen, T. A. Abbott, E. Barrett-Connor, P. D. Miller, L. E. Wehren, and M. L. Berger. “Bone mineral density thresholds for pharmacological intervention to prevent fractures.” In: *Archives of internal medicine* 164.10 (2004), pp. 1108–1112.

[7] M. Ito, K. Ikeda, M. Nishiguchi, H. Shindo, M. Uetani, T. Hosoi, and H. Orimo. “Multi-detector row CT imaging of vertebral microstructure for evaluation of fracture risk.” In: *Journal of Bone and Mineral Research* 20.10 (2005), pp. 1828–1836.

[8] T. M. Link. “Osteoporosis imaging: state of the art and advanced imaging.” In: *Radiology* 263.1 (2012), pp. 3–17.

[9] T. Baum, D. C Karampinos, H. Liebl, E. J Rummeny, S. Waldt, and J. S Bauer. “High-resolution bone imaging for osteoporosis diagnostics and therapy monitoring using clinical MDCT and MRI.” In: *Current medicinal chemistry* 20.38 (2013), pp. 4844–4852.

[10] C. Graeff, W. Timm, T. N. Nickelsen, J. Farrerons, F. Mar ın, C. Barker, and C. C. Glüer. “Monitoring teriparatide-associated changes in vertebral microstructure by high-resolution CT in vivo: Results from the EUROFORS study.” In: *Journal of Bone and Mineral Research* 22.9 (2007), pp. 1426–1433.

[11] J. Radon. “1.1 über die bestimmung von funktionen durch ihre integralwerte längs gewisser mannigfaltigkeiten.” In: *Classic papers in modern diagnostic radiology* 5 (2005), p. 21.

[12] R. N. Bracewell. “Numerical transforms.” In: *Science* 248.4956 (1990), pp. 697–704.

[13] A. C. Kak and M. Slaney. *Principles of computerized tomographic imaging*. IEEE press New York, 1988.

[14] G. Ramachandran and A. Lakshminarayanan. “Three-dimensional reconstruction from radiographs and electron micrographs: application of convolutions instead of Fourier transforms.” In: *Proceedings of the National Academy of Sciences* 68.9 (1971), pp. 2236–2240.

[15] T. Köhler, B. Brendel, and R. Proksa. “Beam shaper with optimized dose utility for helical cone-beam CT.” In: *Medical physics* 38.S1 (2011).

[16] K. Lange, R. Carson, et al. “EM reconstruction algorithms for emission and transmission tomography.” In: *J Comput Assist Tomogr* 8.2 (1984), pp. 306–16.

[17] Y. Vardi, L. Shepp, and L. Kaufman. “A statistical model for positron emission tomography.” In: *Journal of the American statistical Association* 80.389 (1985), pp. 8–20.

[18] M. J. Willemink, P. A. de Jong, T. Leiner, L. M. de Heer, R. A. Nievelstein, R. P. Budde, and A. M. Schilham. “Iterative reconstruction techniques for computed tomography Part 1: technical principles.” In: *European radiology* 23.6 (2013), pp. 1623–1631.

[19] P. B. Noël, A. A. Fingerle, B. Renger, D. Münzel, E. J. Rummeny, and M. Dobritz. “Initial performance characterization of a clinical noise–suppressing reconstruction algorithm for mdct.” In: *American Journal of Roentgenology* 197.6 (2011), pp. 1404–1409.

[20] J. A. Fessler. “Statistical image reconstruction methods for transmission tomography.” In: *Handbook of Medical Imaging* 2 (2000), pp. 1–70.

[21] H. Erdogan. “Statistical image reconstruction algorithms using paraboloidal surrogates for PET transmission scans.” PhD thesis. The University of Michigan, 1999.

[22] K. Lange. “Convergence of EM image reconstruction algorithms with Gibbs smoothing.” In: *IEEE transactions on medical imaging* 9.4 (1990), pp. 439–446.

[23] P. J. Huber et al. “Robust estimation of a location parameter.” In: *The annals of mathematical statistics* 35.1 (1964), pp. 73–101.

[24] K. M. Brown, S. Zabic, and T. Koehler. “Comparison of ML iterative reconstruction and TV-minimization for noise reduction in CT images.” In: *Fully Three-Dimensional Image Reconstruction in Radiology and Nuclear Medicine (Fully 3D, Potsdam, Germany, 2011)* (2011), pp. 443–446.

[25] D. Lira, A. Padole, M. K. Kalra, and S. Singh. “Tube potential and CT radiation dose optimization.” In: *American journal of roentgenology* 204.1 (2015), W4–W10.

[26] E. Y. Sidky and X. Pan. “Image reconstruction in circular cone-beam computed tomography by constrained, total-variation minimization.” In: *Physics in Medicine & Biology* 53.17 (2008), p. 4777.

[27] U. Wiedmann, V. B. Neculaes, D. Harrison, E. Asma, P. E. Kinahan, and B. De Man. “X-ray pulsing methods for reduced-dose computed tomography in PET/CT attenuation correction.” In: *Medical Imaging 2014: Physics of Medical Imaging*. Vol. 9033. International Society for Optics and Photonics. 2014, 90332Z.

[28] GE Healthcare. *InnovaTM 2100-IQ, 3100-IQ, 4100-IQ Cardiovascular Imaging System Operator Manual*. Direction 5391979-5-399 (EN), 2011.

[29] P. Rauch, P.-J. P. Lin, S. Balter, A. Fukuda, A. Goode, G. Hartwell, T. LaFrance, E. Nickoloff, J. Shepard, and K. Strauss. “Functionality and operation of fluoroscopic automatic brightness control/automatic dose rate control logic in modern cardiovascular and interventional angiography systems: A Report of Task Group 125 Radiography/Fluoroscopy Subcommittee, Imaging Physics Committee, Science Council.” In: *Medical physics* 39.5 (2012), pp. 2826–2828.

[30] J. Uribe, J. L. Reynolds, L. P. Inzinna, R. Longtin, D. D. Harrison, B. De Man, B. Neculaes, A. Caiafa, W. Waters, K. J. Frutschy, et al. “Multisource inverse-geometry CT?Prototype system integration.” In: *Nuclear Science Symposium Conference Record (NSS/MIC), 2010 IEEE*. IEEE. 2010, pp. 2578–2581.

[31] R. Huesman. “The effects of a finite number of projection angles and finite lateral sampling of projections on the propagation of statistical errors in transverse section reconstruction.” In: *Physics in Medicine & Biology* 22.3 (1977), p. 511.

[32] J. S. Jorgensen, E. Y. Sidky, and X. Pan. “Quantifying admissible undersampling for sparsity-exploiting iterative image reconstruction in X-ray CT.” In: *IEEE Transactions on Medical Imaging* 32.2 (2013), pp. 460–473.

[33] E. Y. Sidky, C.-M. Kao, and X. Pan. “Accurate image reconstruction from few-views and limited-angle data in divergent-beam CT.” In: *Journal of X-ray Science and Technology* 14.2 (2006), pp. 119–139.

[34] X. Han, J. Bian, E. L. Ritman, E. Y. Sidky, and X. Pan. “Optimization-based reconstruction of sparse images from few-view projections.” In: *Physics in Medicine & Biology* 57.16 (2012), p. 5245.

[35] S. Abbas, T. Lee, S. Shin, R. Lee, and S. Cho. “Effects of sparse sampling schemes on image quality in low-dose CT.” In: *Medical physics* 40.11 (2013).

[36] S. Abbas, J. Min, and S. Cho. “Super-sparsely view-sampled cone-beam CT by incorporating prior data.” In: *Journal of X-ray science and technology* 21.1 (2013), pp. 71–83.

[37] J. Bian, J. H. Siewerdsen, X. Han, E. Y. Sidky, J. L. Prince, C. A. Pelizzari, and X. Pan. “Evaluation of sparse-view reconstruction from flat-panel-detector cone-beam CT.” In: *Physics in Medicine & Biology* 55.22 (2010), p. 6575.

[38] Z. Zhao, G. Gang, and J. Siewerdsen. “Noise, sampling, and the number of projections in cone-beam CT with a flat-panel detector.” In: *Medical physics* 41.6Part1 (2014).

[39] A. Sisniega, W. Zbijewski, J. Stayman, J. Xu, K. Taguchi, E. Fredenberg, M. Lundqvist, and J. Siewerdsen. “Volumetric CT with sparse detector arrays (and application to Si-strip photon counters).” In: *Physics in Medicine & Biology* 61.1 (2015), p. 90.

[40] G. J. Gang, J. H. Siewerdsen, and J. W. Stayman. “Task-driven optimization of CT tube current modulation and regularization in model-based iterative reconstruction.” In: *Physics in Medicine & Biology* 62.12 (2017), p. 4777.

[41] G. J. Gang, J. H. Siewerdsen, and J. W. Stayman. “Task-Driven Optimization of Fluence Field and Regularization for Model-Based Iterative Reconstruction in Computed Tomography.” In: *IEEE transactions on medical imaging* 36.12 (2017), pp. 2424–2435.

[42] T. Koesters, F. Knoll, A. Sodickson, D. K. Sodickson, and R. Otazo. “SparseCT: interrupted-beam acquisition and sparse reconstruction for radiation dose reduction.” In: *Medical Imaging 2017: Physics of Medical Imaging*. Vol. 10132. International Society for Optics and Photonics. 2017, 101320Q.

[43] B. Chen, M. Muckley, A. Sodickson, T. O’Donnell, F. Knoll, D. Sodickson, and R. Otazo. “Evaluation of SparseCT on patient data using realistic undersampling models.” In: *Medical Imaging 2018: Physics of Medical Imaging*. Vol. 10573. International Society for Optics and Photonics. 2018, p. 1057342.

[44] M. Muckley, B. Chen, T. O’Donnell, m. Berner, T. Allmendinger, K. Stierstorfer, T. Flohr, B. Schmidt, A. Sodickson, D. Sodickson, and R. Otazo. “Reconstruction of Reduced-Dose SparseCT Data Acquired With An Interrupted-Beam Prototype On A Clinical Scanner.” In: *5th CT Meeting*. 2018.

[45] S. Žabić, Q. Wang, T. Morton, and K. M. Brown. “A low dose simulation tool for CT systems with energy integrating detectors.” In: *Medical physics* 40.3 (2013).

[46] D. Muenzel, T. Koehler, K. Brown, S. Žabić, A. A. Fingerle, S. Waldt, E. Bendik, T. Zahel, A. Schneider, M. Dobritz, et al. “Validation of a low dose simulation technique for computed tomography images.” In: *PloS one* 9.9 (2014), e107843.

[47] Mindway Software. *QCT Pro Bone Mineral Densitometry Software, Phantom Module. Version 4.* 2005.

[48] T. Baum, D. Müller, M. Dobritz, E. J. Rummeny, T. M. Link, and J. S. Bauer. “BMD measurements of the spine derived from sagittal reformations of contrast-enhanced MDCT without dedicated software.” In: *European journal of radiology* 80.2 (2011), e140–e145.

[49] T. Baum, M. Gräbeldinger, C. Räth, E. G. Garcia, R. Burgkart, J. M. Patsch, E. J. Rummeny, T. M. Link, and J. S. Bauer. “Trabecular bone structure analysis of the spine using clinical MDCT: can it predict vertebral bone strength?” In: *Journal of bone and mineral metabolism* 32.1 (2014), pp. 56–64.

[50] T. Baum, J. Carballido-Gamio, M. Huber, D. Müller, R. Monetti, C. Räth, F. Eckstein, E. Lochmüller, S. Majumdar, E. Rummeny, et al. “Automated 3D trabecular bone structure analysis of the proximal femur?prediction of biomechanical strength by CT and DXA.” In: *Osteoporosis international* 21.9 (2010), pp. 1553–1564.

[51] S. Majumdar, H. Genant, S. Grampp, D. Newitt, V.-H. Truong, J. Lin, and A. Mathur. “Correlation of trabecular bone structure with age, bone mineral density, and osteoporotic status: in vivo studies in the distal radius using high resolution magnetic resonance imaging.” In: *Journal of Bone and Mineral Research* 12.1 (1997), pp. 111–118.

[52] R. D. Evans and R. Evans. “The atomic nucleus.” In: (1955).

[53] A. H. Compton. “A quantum theory of the scattering of X-rays by light elements.” In: *Physical review* 21.5 (1923), p. 483.

[54] J. W. Strutt. “LVIII. On the scattering of light by small particles.” In: *The London, Edinburgh, and Dublin Philosophical Magazine and Journal of Science* 41.275 (1871), pp. 447–454.

[55] L. Lehmann, R. Alvarez, A. Macovski, W. Brody, N. Pelc, S. J. Riederer, and A. Hall. “Generalized image combinations in dual KVP digital radiography.” In: *Medical physics* 8.5 (1981), pp. 659–667.

[56] B. Heismann, J. Leppert, and K. Stierstorfer. “Density and atomic number measurements with spectral x-ray attenuation method.” In: *Journal of applied physics* 94.3 (2003), pp. 2073–2079.

[57] O. Klein and Y. Nishina. “Über die Streuung von Strahlung durch freie Elektronen nach der neuen relativistischen Quantendynamik von Dirac.” In: *Zeitschrift für Physik* 52.11-12 (1929), pp. 853–868.

[58] X. Duan, J. Wang, L. Yu, S. Leng, and C. H. McCollough. “CT scanner x-ray spectrum estimation from transmission measurements.” In: *Medical physics* 38.2 (2011), pp. 993–997.

[59] T. R. Fewell, R. E. Shuping, and K. R. Hawkins. *Handbook of computed tomography x-ray spectra*. US Department of Health, Human Services, Public Health Service, Food, and Drug Administration, Bureau of Radiological Health, 1981.

[60] J. M. Boone and J. A. Seibert. “An accurate method for computer-generating tungsten anode x-ray spectra from 30 to 140 kV.” In: *Medical physics* 24.11 (1997), pp. 1661–1670.

[61] Siemens Healthcare GmbH. *Simulation of X-ray Spectra: Online tool for the simulation of X-ray Spectra*. 2019. URL: https://www.oem-xray-components.siemens.com/x-ray-spectra-simulation.

[62] L. Yu, S. Leng, and C. H. McCollough. “Dual-energy CT–based monochromatic imaging.” In: *American journal of Roentgenology* 199.5_supplement (2012), S9–S15.

[63] M. Saito. “Potential of dual-energy subtraction for converting CT numbers to electron density based on a single linear relationship.” In: *Medical physics* 39.4 (2012), pp. 2021–2030.

[64] M. Tsukihara, Y. Noto, T. Hayakawa, and M. Saito. “Conversion of the energy-subtracted CT number to electron density based on a single linear relationship: an experimental verification using a clinical dual-source CT scanner.” In: *Physics in Medicine & Biology* 58.9 (2013), N135.